Determination of Optimal Shot Peen Forming Patterns Using the Theory of Non-Euclidean Plates

Vladislav Sushitskii[1]
Laboratory of Multiscale Mechanics (LM2),
Aluminium Research Center (REGAL),
Polytechnique Montreal,
Montreal, QC H3T1J4, Canada
e-mail: vladislav.sushitskii@polymtl.ca

Wim M. van Rees
Assistant Professor
Department of Mechanical Engineering,
Massachusetts Institute of Technology,
Cambridge, MA 02139-4307
e-mail: wvanrees@mit.edu

Martin Levesque
Professor
Laboratory of Multiscale Mechanics (LM2),
Aluminium Research Center (REGAL),
Polytechnique Montreal,
Montreal, QC H3T1J4, Canada
e-mail: martin.levesque@polymtl.ca

Frederick P. Gosselin
Associate Professor
Laboratory of Multiscale Mechanics (LM2),
Aluminium Research Center (REGAL),
Polytechnique Montreal,
Montreal, QC H3T1J4, Canada
e-mail: frederick.gosselin@polymtl.ca

Determination of Optimal Shot Peen Forming Patterns Using the Theory of Non-Euclidean Plates

We show how a theoretical framework developed for modeling nonuniform growth can model the shot peen forming process. Shot peen forming consists in bombarding a metal panel with multiple millimeter-sized shots that induce local bending of the panel. When applied to different areas of the panel, peen forming generates compound curvature profiles starting from a flat state. We present a theoretical approach and its practical realization for simulating peen forming numerically. To achieve this, we represent the panel undergoing peen forming as a bilayer plate, and we apply a geometry-based theory of non-Euclidean plates to describe its reconfiguration. Our programming code based on this approach solves two types of problems: it simulates the effect of a predefined treatment (the forward problem) and it finds the optimal treatment to achieve a predefined target shape (the inverse problem). Both problems admit using multiple peening regimes simultaneously. The algorithm was tested numerically on 200 randomly generated test cases.
[DOI: 10.1115/1.4056072]

Keywords: modeling and simulation, process planning, sheet and tube metal forming

1 Introduction

Shot peen forming is a cost-effective technology for shaping large metal plates, such as airplane wing skins, without dies. It consists in bombarding the surface of a component with a large number of millimeter-sized shots made of steel, glass, or ceramic. The velocity of a shot is sufficiently high to plastically deform the upper layer of the plate upon impact and to stretch the plate locally. This effect causes local bending of thin components and leads to a convex curvature on the peened side [1]. Repeated impacts also induce a field of compressive residual stress that can improve fatigue life [2].

When developing a shot peen forming process, one is faced with two types of problems as schematized in Fig. 1:*the forward problem* and *the inverse problem* [3]. The forward problem is formulated with the following question: Which shape will the component adopt if it is peened according to a given pattern? The inverse problem denotes the following: Given an initial shape of the component and the target shape, how should one peen the component to make it deform into the target shape? A numerical solver for both problems is necessary to optimize the forming process. Thus, without numerical resolution of the inverse problem, the design of a peen forming procedure for each new component is a craft trial-and-error process plagued with risk and uncertainty. It lasts up to several months and implies many scrapped parts. On the other hand, numerical resolution of the forward problem is necessary to check the quality of the inverse problem resolution and to simulate the effect of additional treatments.

A straightforward simulation of individual peening impact, such as the one conducted in Ref. [4], is precise but computationally expensive. For this reason, simplified multiscale simulation approaches, such as the *eigenstrain* approach, were developed. It implies formulating the applied peening loads in terms of non-elastic strains imposed on the component [5,6]. The eigenstrain approach represents the treated plate as a thin bilayer where each layer undergoes a nonuniform plastic in-plane swelling or shrinking. The forward problem in this formulation can be numerically solved using shell finite element models [7,8]. In addition, such models allow to implement an inverse problem resolution algorithm based on the topology optimization methods [9,10]. A similar inverse problem resolution approach was also applied in Ref. [11] in the context of the *laser* peen forming process. Given that this method is based on numerical optimization, its speed decreases with the number of elements in the model. On the other hand, the inverse problem can be solved using an artificial neural network [8]. The neural network provides near-perfect accuracy and fast calculation on-line. However, it requires the generation of a large finite element forward problem solution database and a long training phase for each new plate geometry.

To overcome these issues during the inverse problem resolution, we turned to the theory of non-Euclidean plates [12,13]. This theoretical framework lies at the intersection of mechanics and differential geometry. It precisely describes distortion of multilayer plates induced by the prescription of a nonuniform non-elastic strain. Prescription of such strain makes the surface metric non-Euclidean so that it does not satisfy the compatibility conditions of the Euclidean space, which gives name to the theory [13]. Experiments conducted in the field of 4D printing with elastic polymer sheets have proven the accuracy of the theory of non-Euclidean plates in numerical forward problem resolution. Thus, this theory precisely predicted curvature of spherical, cylindrical, and saddle shapes grown out of a flat state by induction of a nonuniform plastic strain [14,15]. Numerical simulation of growth for these three cases also showed good accordance with analytical shapes [16]. Moreover, this theory predicted the form of more complex shapes, such as helicoid, catenoid, or an orchid flower grown out of a flat state using polymer bilayers with oriented filaments [17]. The theory of non-Euclidean plates also provides instruments for an efficient inverse problem

[1]Corresponding author.
Manuscript received October 18, 2021; final manuscript received October 21, 2022; published online December 2, 2022. Assoc. Editor: Steven Schmid.

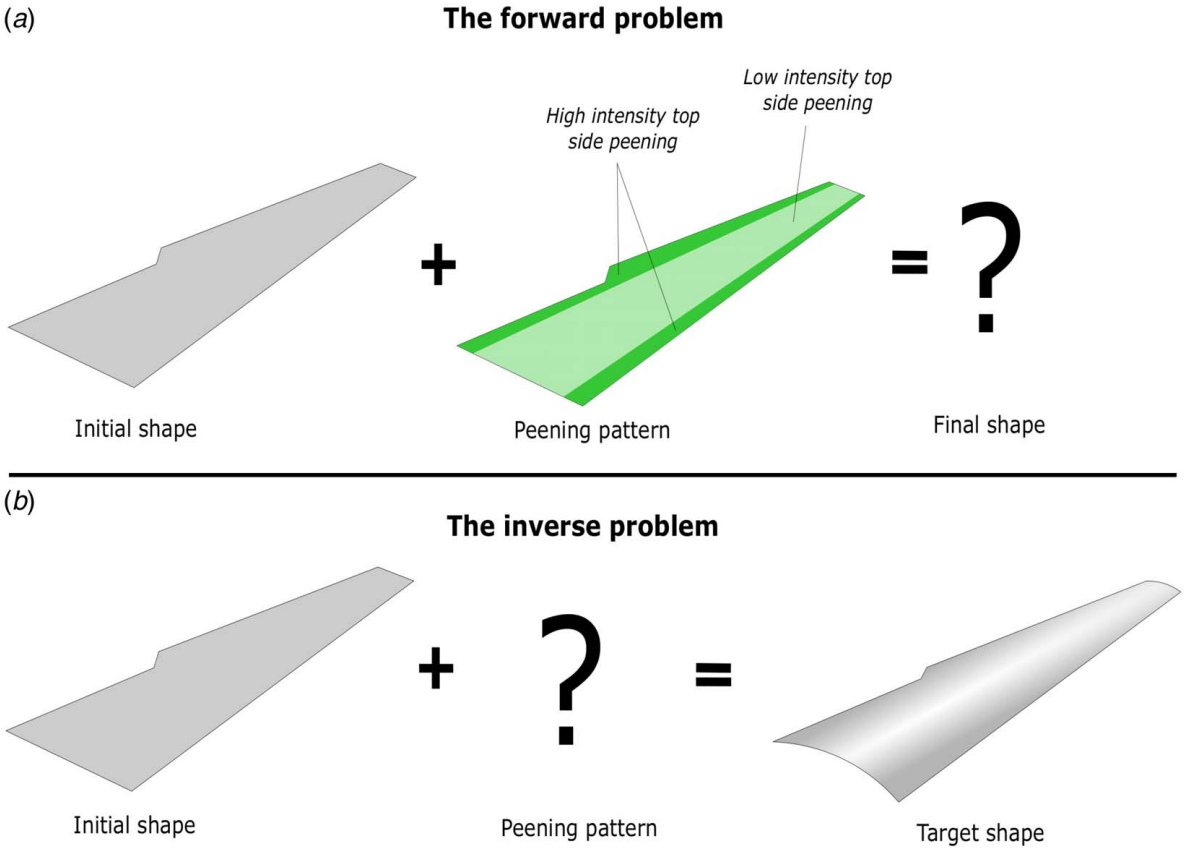

Fig. 1 The two problems of the shot peen forming simulation: (*a*) The forward problem consists in the determination of the final shape of the component given its initial shape and the peening pattern and (*b*) The inverse problem consists in determination of the optimal peening pattern given the initial shape of the component and its target shape

resolution. Such algorithms for the case of polymers with oriented local growth are reported in Refs. [17,18].

In this paper, we propose to use the eigenstrain approach to represent the treated plate as a bilayer, and we resort to the theory of non-Euclidean plates to calculate the resulting distortion of the bilayer. To numerically solve the inverse problem, we created an iterative algorithm that implies resolving the forward problem on each iteration. The algorithm adjusts the peening pattern based on the discrepancy between the current shape, i.e., the shape obtained with the current pattern, and the target shape. The adjustment is done on a local scale using simple arithmetic operations, so the computation speed on this stage stays constant with an increasing number of variables. This stage does not require any preliminary training phase either. The algorithm constitutes a general approach for the inverse problem resolution in case of bilayers subjected to isotropic, i.e., non-oriented, local growth, such as those examined in Ref. [15]. When the iterative adjustment is finished, we group the peening pattern to make it practically applicable. In other words, we divide the pattern into zones treated with constant peening regimes. The number of available peening regimes and their intensities are predetermined based on the practical constraints.

We start this paper with the theoretical background section. First, we examine the eigenstrain approach that relates peen formed plates and swelling non-Euclidean bilayers. Next, we move to the theory of non-Euclidean plates, namely to the geometrical shape description and the forward problem resolution method that it implies. In this section we also formulate the inverse problem in terms of the theory of non-Euclidean plates. We then pass to the methodology section by presenting our inverse problem resolution algorithm and an approach for its numerical implementation. The grouping and validation strategies are presented in the same section. The results of the validation campaign are presented subsequently, and finally the advantages and limitations of our approach are discussed.

2 Theoretical Background

2.1 The Eigenstrain Approach and Strain Decomposition. The term eigenstrains denotes all non-elastic strains arising in the material, such as plastic, thermal, or piezoelectric strains [5]. The only type of eigenstrain generated by peen forming is the plastic strain. Indeed, numerous overlapping impact indentations plastically stretch the outer layer of the material, and the rest of the material responds to this newly introduced eigenstrain with the emergence of stress. In order to conserve its integrity and to balance the stress, the plate deforms elastically. In case of small strains, the residual strain tensor $\boldsymbol{\varepsilon}^{\text{res}}$ is additively decomposed into the eigenstrain part $\boldsymbol{\varepsilon}$ and the elastic part $\boldsymbol{\varepsilon}^{\text{el}}$ ([19] and Appendix):

$$\boldsymbol{\varepsilon}^{\text{res}} = \boldsymbol{\varepsilon} + \boldsymbol{\varepsilon}^{\text{el}} \tag{1}$$

This relation holds for peen forming because the process deals with thin plates and the peening-induced strains are small [4]. The elastic strain may affect the whole plate, while the eigenstrain is present only in the stretched outer layer. The thickness of the plastically deformed outer layer varies depending on the peening parameters and the treated material. With the eigenstrain approach, the resolution of the forward problem for shot peen forming consists in introducing the eigenstrain over the whole shot peened area and determining the elastic springback.

2.1.1 The Through-Thickness Eigenstrain Profile. We endow the mid-surface of the plate with two Lagrangian coordinates (x, y), and we assign a Lagrangian coordinate z in the through-thickness direction. The Lagrangian coordinates follow the plate as it deforms. We assume that the material is plastically isotropic, so the eigenstrains are the same in all in-plane directions: $\varepsilon_{xx}(x, y, z) = \varepsilon_{yy}(x, y, z)$. Also, $\varepsilon_{zz} = -2\varepsilon_{xx}$ due to plastic incompressibility. For a

small area around a point (x_0, y_0) on the mid-surface, the through-thickness eigenstrain profile $\varepsilon_{xx}(x_0, y_0, z) = \varepsilon_{yy}(x_0, y_0, z)$ can be measured directly using the X-ray diffraction method [20]. Otherwise, it can be deduced from the residual stress profile, which is determined with such methods as hole drilling [21], layer-removal [21,22], or the two cut compliance method [23]. In this case, the through-thickness eigenstrain profile is optimized using numerical simulations in a way that the generated residual stress profile corresponds to the experimentally measured one [7,24]. With this, the correspondence between the peening regimes and the induced eigenstrains can be established by treating identical experimental specimens with varying process parameters and determining the induced eigenstrains. If the forming procedure implies subsequent treatment of the same area with different peening regimes, then, in terms of eigenstrains, such a combined treatment can be considered as an additional peening regime.

Mechanically, the introduction of the eigenstrain can be modeled as slicing the plate into thin layers, stretching the outer layers separately following the eigenstrain profile, and then gluing everything back. To numerically simplify the problem, we virtually idealize the eigenstrain profile by assuming that the plate consists of two layers of equal thickness that can separately undergo nonuniform in-plane swelling or shrinking. The idealized eigenstrain profile leads to the same deformed shape as the real one. Figure 2 illustrates both profiles induced on a uniformly treated plate. Mathematically, the idealization procedure consists in finding the local eigenstrain $\varepsilon^t(x, y)$ to be introduced in the top layer and the local eigenstrain $\varepsilon^b(x, y)$ to be introduced in the bottom layer. It is done by equating the total eigenstrain $\Gamma(x, y)$ [6] and the first eigenstrain moment $\Gamma_1(x, y)$ [6] induced locally by the real eigenstrain profile to those induced locally by $\varepsilon^t(x, y)$ and $\varepsilon^b(x, y)$. In the general case, Γ and Γ_1 are defined as

$$\Gamma(x, y) = \int_{-h/2}^{h/2} \varepsilon_{xx}(x, y, z)\, \mathrm{d}z \tag{2}$$

$$\Gamma_1(x, y) = \int_{-h/2}^{h/2} \varepsilon_{xx}(x, y, z) z\, \mathrm{d}z \tag{3}$$

where h stands for the plate thickness. For the idealized bilayer, profile Γ and Γ_1 are expressed as

$$\Gamma(x, y) = \frac{h}{2}\left(\varepsilon^t(x, y) + \varepsilon^b(x, y)\right) \tag{4}$$

$$\Gamma_1(x, y) = \frac{h^2}{8}\left(\varepsilon^t(x, y) - \varepsilon^b(x, y)\right) \tag{5}$$

The idealized eigenstrain is positive on the side that undergoes the peening treatment and is negative on the other side. It should be noted that although ε^t and ε^b give rise to the same in-plane extension and curvature as the real eigenstrain profile, the idealized one generates a different residual stress profile [7]. Indeed, the linear elasticity theory expresses the components of the residual stress tensor $\boldsymbol{\sigma}$ through the components of the elastic strain tensor $\boldsymbol{\varepsilon}^{\mathrm{el}}$ [6]:

$$\begin{cases} \sigma_{xx} = \frac{Y}{1-\nu^2}\left(\varepsilon^{\mathrm{el}}_{xx} + \nu\varepsilon^{\mathrm{el}}_{yy}\right) \\ \sigma_{yy} = \frac{Y}{1-\nu^2}\left(\varepsilon^{\mathrm{el}}_{yy} + \nu\varepsilon^{\mathrm{el}}_{xx}\right) \end{cases} \tag{6}$$

The elastic strain tensor, in turn, is influenced by the eigenstrain tensor (see Eq. (1)).

2.2 The Theory of Non-Euclidean Plates Applied to the Modeling of Shot Peen Forming. The theory of non-Euclidean plates allows to numerically determine the elastic response of thin bodies to an applied nonuniform non-elastic strain, e.g., eigenstrain. If the plate fully incorporates the prescribed eigenstrain, so that $\boldsymbol{\varepsilon}^{\mathrm{res}} = \boldsymbol{\varepsilon}$ and $\boldsymbol{\sigma} = 0$, then it adopts a so-called *rest configuration*. The prescribed eigenstrains can be incompatible, meaning that the plate can not adopt the rest configuration without the loss of integrity. In this case, a solid plate adopts an integral *final configuration (final shape)* by compensating the eigenstrains with the elastic strains, which is the case of peen forming. The presence of elastic strains, in turn, leads to the emergence of residual stresses.

Once assigned with a rest configuration, the plate adopts a final configuration that minimizes its global elastic energy [12,13]. Hence, if the global elastic energy has multiple global minima, then the final configuration is not unique. In turn, the same final configuration can be induced by different rest configurations. Moreover, during morphing, the plate can get stuck in a configuration corresponding to a local minimum on its way to the final configuration corresponding to the global minimum [19]. The theory of non-Euclidean paves a way to explore the relation between the rest and the final configurations in all cases and uses tools from differential geometry to describe the shape of plates. In terms of numerical implementation, we adopted the approach described in Ref. [19].

2.2.1 Geometrical Shape Description. In the framework of the theory of non-Euclidean plates, the plate shape is associated with the shape of its mid-surface [19]. We denote by U the domain of the plane containing the coordinates (x, y) that parameterize the mid-surface: $(x, y) \in U \subset \mathbb{R}^2$. The position of each point of the mid-surface in a 3D space is defined by the mapping $\vec{m}: U \to \mathbb{R}^3$. We adopt the Kirchhoff-Love assumptions, so the position $\vec{r}$ of a point belonging to the plate is expressed as

$$\vec{r}(x, y, z) = \vec{m}(x, y) + z\vec{n}(x, y) \tag{7}$$

where $\vec{n}$ is the unit normal vector. The mid-surface shape is described by *the first and the second fundamental forms*, that are binary quadratic forms associated with a symmetric 2×2 matrix. Both fundamental forms are local quantities varying smoothly along the surface. The first fundamental form describes changes in the length of curves and areas of regions on the surface. In other words, it describes the local stretching of the surface. The 2×2 matrix containing coefficients of the first fundamental form $\mathbf{a}(x, y)$ is computed as

$$\mathbf{a}(x, y) = \begin{bmatrix} \partial_x\vec{m} \cdot \partial_x\vec{m} & \partial_x\vec{m} \cdot \partial_y\vec{m} \\ \partial_y\vec{m} \cdot \partial_x\vec{m} & \partial_y\vec{m} \cdot \partial_y\vec{m} \end{bmatrix} \tag{8}$$

where $\partial_x\vec{m} = \partial\vec{m}/\partial x$ and $\partial_y\vec{m} = \partial\vec{m}/\partial y$ are two vectors tangent to the mid-surface at the point $\vec{m}(x, y)$. If a certain area of the surface does not undergo any stretching, the first fundamental form in this area is represented by the identity matrix $\mathbf{I}$.

Together with the first fundamental form, the second fundamental form determines local curvatures on a surface. The matrix containing its coefficients $\mathbf{b}(x, y)$ is computed as

$$\begin{aligned} \mathbf{b}(x, y) &= \begin{bmatrix} \partial_{xx}\vec{m} \cdot \vec{n} & \partial_{xy}\vec{m} \cdot \vec{n} \\ \partial_{xy}\vec{m} \cdot \vec{n} & \partial_{yy}\vec{m} \cdot \vec{n} \end{bmatrix} \\ &= \begin{bmatrix} \partial_x(\partial_x\vec{m} \cdot \vec{n}) - \partial_x\vec{m} \cdot \partial_x\vec{n} & \partial_y(\partial_x\vec{m} \cdot \vec{n}) - \partial_x\vec{m} \cdot \partial_y\vec{n} \\ \partial_y(\partial_x\vec{m} \cdot \vec{n}) - \partial_x\vec{m} \cdot \partial_y\vec{n} & \partial_y(\partial_y\vec{m} \cdot \vec{n}) - \partial_y\vec{m} \cdot \partial_y\vec{n} \end{bmatrix} \\ &= -\begin{bmatrix} \partial_x\vec{m} \cdot \partial_x\vec{n} & \partial_x\vec{m} \cdot \partial_y\vec{n} \\ \partial_x\vec{m} \cdot \partial_y\vec{n} & \partial_y\vec{m} \cdot \partial_y\vec{n} \end{bmatrix} \end{aligned} \tag{9}$$

where $\partial_{xx}\vec{m}$, $\partial_{xy}\vec{m}$, and $\partial_{yy}\vec{m}$ denote the second derivatives of $\vec{m}(x, y)$, and the last equality is obtained using the orthogonality of the tangent and normal vectors. If a surface is locally flat, its second fundamental form at this area is described by the zero matrix, because the derivatives of the tangent and normal vectors equal zero.

The two fundamental forms define a unique surface up to rigid body motions. The surface is integral if its fundamental forms are *compatible*, i.e., if they satisfy three partial differential equations

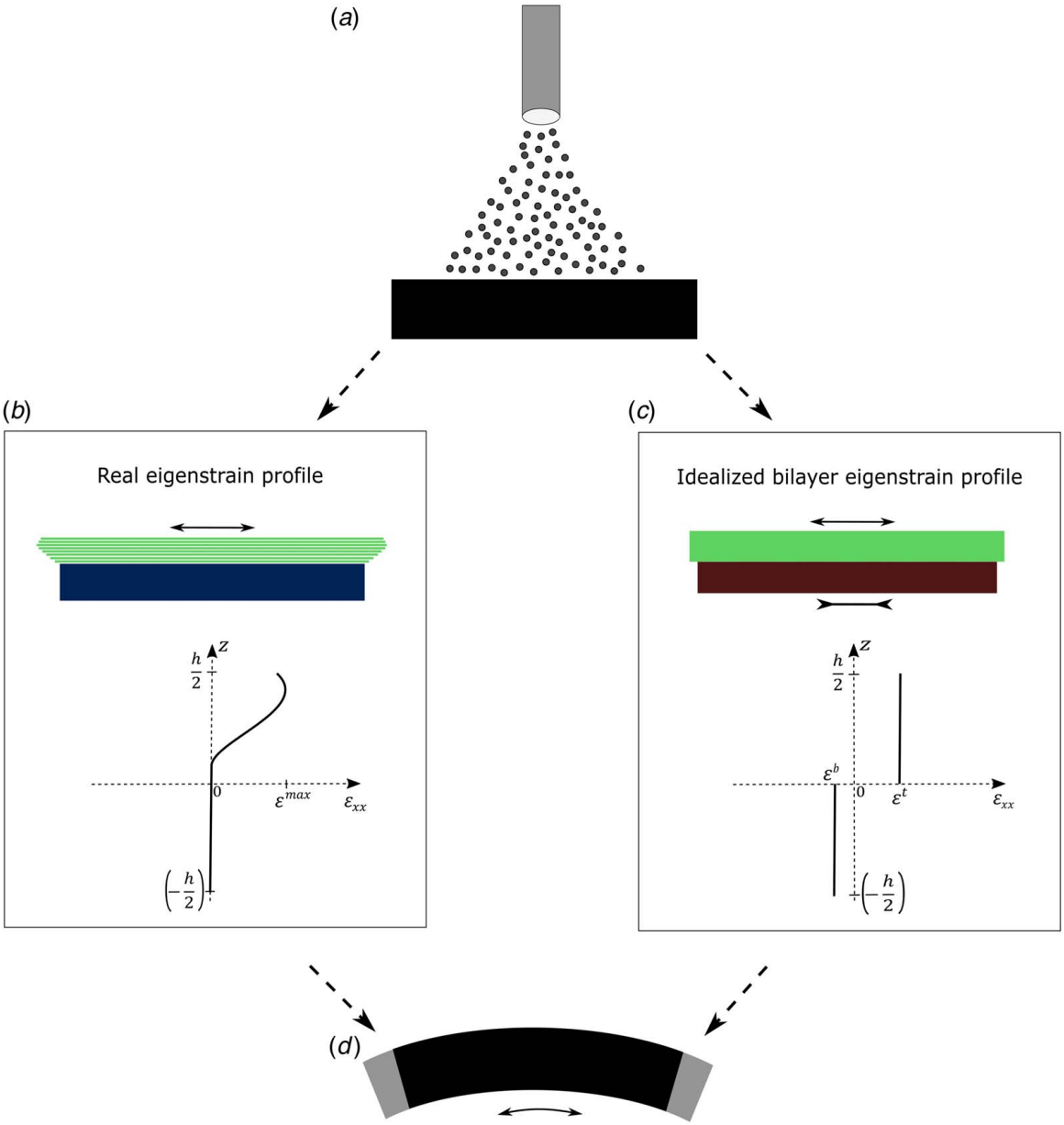

Fig. 2 The real and idealized eigenstrain profiles induced by uniform shot peening of a plate. We denote the plate thickness as *h*. The coordinate *z* goes along the thickness and measures from the midplane: (*a*) The plate undergoes uniform shot peening (side view), (*b*) The through-thickness eigenstrain profile is nonuniform along *z*, and its peak value ε^{max} is close to the surface [7]. Its effect is accurately simulated by virtually dividing the plate into thin layers and imposing different eigenstrain to each of the layers thus reproducing the profile shape, (c) We idealize the eigenstrain profile and represent the plate as a bilayer consisting of two layers of thickness *h*/2. The eigenstrain ε^t and ε^b assigned to each of the layers is derived from the real eigenstrain profile by equating the total eigenstrain and the first eigenstrain moment and (*d*) Both real and idealized eigenstrain profiles lead to the same deformed shape, which is bent and stretched with respect to the initial state.

called the Gauss–Peterson–Mainardi–Codazzi equations, which can be found, for instance, in Ref. [25]. Hence, the two *final* fundamental forms of a non-Euclidean plate are compatible, while its *rest* fundamental forms are not. This phenomenon illustrated in Fig. 3 is also called *geometric incompatibility*.

2.2.2 Elastic Energy and the Forward Problem Resolution. In terms of the theory of non-Euclidean plates, the forward problem consists in determining the final configuration as a function of the rest configuration. First, we consider the simple case of an initially flat *monolayer* plate, which is subjected to a rest configuration described by the incompatible fundamental forms $\mathbf{a}_r$ and $\mathbf{b}_r$. The rest and final configurations of such a plate are related through the elastic energy functional. We denote the final fundamental forms as $\mathbf{a}_f$ and $\mathbf{b}_f$ and we express the elastic energy E_{ML} of an integral monolayer plate as [19]

$$E_{\mathrm{ML}} = \frac{1}{2}\int_U \left[\frac{h}{4}\left\|\mathbf{a}_r^{-1}\mathbf{a}_f - \mathbf{I}\right\|_e^2 + \frac{h^3}{12}\left\|\mathbf{a}_r^{-1}(\mathbf{b}_f - \mathbf{b}_r)\right\|_e^2\right]\sqrt{\det \mathbf{a}_r}\,\mathrm{d}x\mathrm{d}y \tag{10}$$

In this expression we have introduced the elastic norm $\|\mathbf{A}\|_e^2 = \alpha Tr^2(\mathbf{A}) + 2\beta Tr(\mathbf{A}^2)$ with coefficients $\alpha = Y\nu/(1-\nu^2)$ and $\beta = Y/(2+2\nu)$. Here, Y is the Young modulus and ν is the Poisson's ratio.

A zero elastic energy means that the final configuration perfectly coincides with the rest one. If the rest fundamental forms are incompatible, an integral plate adopts an equilibrated final configuration

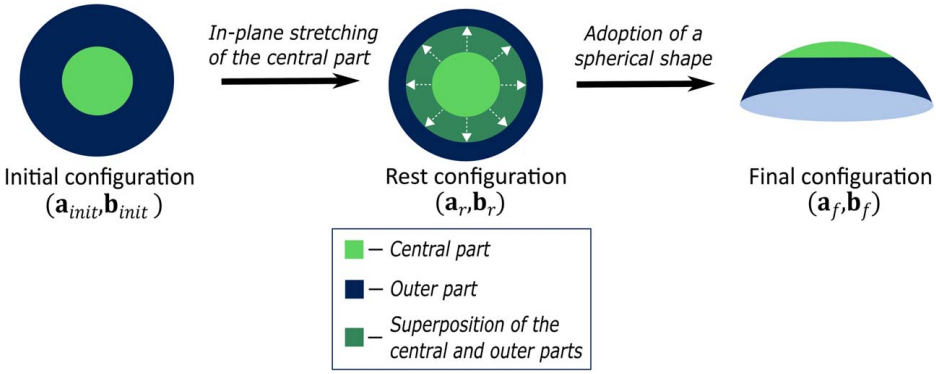

Fig. 3 An example of geometric incompatibility inspired by Pezzulla et al. [14]. The initial configuration described by the fundamental forms (a_{init}, b_{init}) is a flat unstretched disc, so that a_{init} is the identity matrix and b_{init} is the zero matrix along the whole surface. The rest configuration (a_r, b_r) prescribes isotropic in-plane stretching of the central part while conserving the flat shape, so that $a_r \neq a_{init}$ and $b_r = b_{init}$. In the general case, b_r can be different from b_{init} as well. The rest fundamental forms are incompatible, because the adoption of the rest configuration means superposition of the inner part and the outer part of the disc and thus loss of integrity. In order to conserve its integrity, the disc adopts a curved final configuration (a_f, b_f) described by compatible fundamental forms. However, the disc stays residually stressed in its final configuration.

that minimizes the elastic energy under constraints that $\mathbf{a}_f$ and $\mathbf{b}_f$ be compatible. The first term of the elastic energy functional represents the stretching energy, and the second term defines the bending energy. If the plate is thin, the bending term is small in comparison to the stretching one, so the plate stretches as prescribed by the rest configuration but adopts a different curvature. In other words, $\mathbf{a}_f$ in this case is close to $\mathbf{a}_r$, but $\mathbf{b}_f$ can be largely different from $\mathbf{b}_r$. On the contrary, a thick plate adopts the curvature prescribed by the rest configuration but stretches in a different way, so that $\mathbf{b}_f$ is close to $\mathbf{b}_r$ [12].

Now let us consider a *bilayer* plate, where each layer is of thickness $h/2$. We suppose that the plate is initially flat, and that its layers exhibit nonuniform in-plane swelling or shrinking. The eigenstrain introduced in each layer may vary along the surface, but it is constant along the layer thickness. Locally, the eigenstrain is different for each layer, so that the rest first fundamental forms of each layer ($\mathbf{a}_{r,t}$ and $\mathbf{a}_{r,b}$) are different. Matrices $\mathbf{a}_{r,t}$ and $\mathbf{a}_{r,b}$ contain information on the principal eigenstrain direction and magnitude on the top and bottom layers, respectively. Essentially, the $\mathbf{a}_{r,t}$ and $\mathbf{a}_{r,b}$ describe stretching that the layers would adopt if they were not attached together. By assuming that each layer expands uniformly across its thickness, all terms of the rest second fundamental form of each layer are zero along the whole surface:

$$\mathbf{b}_{r,t} = \mathbf{b}_{r,b} = \begin{bmatrix} 0 & 0 \\ 0 & 0 \end{bmatrix} \tag{11}$$

Accordingly, $\mathbf{a}_{r,t}$ and $\mathbf{a}_{r,b}$ fully describe the rest configuration. The forward problem consists in finding $\mathbf{a}_f$ and $\mathbf{b}_f$ that describe the shape of the integral plate mid-surface after reconfiguration. The reconfiguration process for the bilayer case is presented in Fig. 4. Following Ref. [19], we express the elastic energy of the bilayer plate as the sum of the elastic energies of two monolayers of thickness $h/2$. After integration over the total plate thickness, we obtain

$$\begin{aligned} E_{\mathrm{BL}} = \frac{1}{2}\int_U \Big[& \frac{h}{8}\left\|\mathbf{a}_{r,b}^{-1}\mathbf{a}_f - \mathbf{I}\right\|_e^2 + \frac{h^3}{24}\left\|\mathbf{a}_{r,b}^{-1}\mathbf{b}_f\right\|_e^2 \\ & + \frac{h^2}{8}\left\langle \left(\mathbf{a}_{r,b}^{-1}\mathbf{a}_f - \mathbf{I}\right), \mathbf{a}_{r,b}^{-1}\mathbf{b}_f \right\rangle_e \Big] \sqrt{\det\, \mathbf{a}_{r,b}}\, \mathrm{d}x\, \mathrm{d}y \\ & + \frac{1}{2}\int_U \Big[\frac{h}{8}\left\|\mathbf{a}_{r,t}^{-1}\mathbf{a}_f - \mathbf{I}\right\|_e^2 + \frac{h^3}{24}\left\|\mathbf{a}_{r,t}^{-1}\mathbf{b}_f\right\|_e^2 \\ & - \frac{h^2}{8}\left\langle \left(\mathbf{a}_{r,t}^{-1}\mathbf{a}_f - \mathbf{I}\right), \mathbf{a}_{r,t}^{-1}\mathbf{b}_f \right\rangle_e \Big] \sqrt{\det\, \mathbf{a}_{r,t}}\, \mathrm{d}x\, \mathrm{d}y \end{aligned} \tag{12}$$

The elastic energy inner product $\langle \cdot, \cdot \rangle_e$ introduced in this context defines the following operation: $\langle \mathbf{A}, \mathbf{B} \rangle_e = \alpha Tr(\mathbf{A})Tr(\mathbf{B}) + 2\beta Tr(\mathbf{AB})$. Similarly to the monolayer case, the plate adopts a curved final configuration ($\mathbf{a}_f$, $\mathbf{b}_f$) that minimizes the elastic energy. Generally, the final configuration is not unique, and moreover, the plate can get stuck in a configuration corresponding to a local energetic minimum on its way to the global minimum.

For a bilayer subjected to any rest configuration ($\mathbf{a}_{r,b}$, $\mathbf{a}_{r,t}$), there exists an equivalent monolayer that morphs into the same final configuration ($\mathbf{a}_f$, $\mathbf{b}_f$) after being subjected to a rest configuration ($\mathbf{a}_r$, $\mathbf{b}_r$). The relation between ($\mathbf{a}_{r,b}$, $\mathbf{a}_{r,t}$) and ($\mathbf{a}_r$, $\mathbf{b}_r$) is derived by equating the monolayer energy (Eq. (10)) and the bilayer energy (Eq. (12)) and is expressed as [19]

$$\begin{cases} \mathbf{a}_r = \frac{1}{2}\left(\mathbf{a}_{r,b} + \mathbf{a}_{r,t}\right) \\ \mathbf{b}_r = \frac{3}{4h}\left(\mathbf{a}_{r,b} - \mathbf{a}_{r,t}\right) \end{cases} \tag{13}$$

Inversely,

$$\begin{cases} \mathbf{a}_{r,t} = \mathbf{a}_r - \frac{2h}{3}\mathbf{b}_r \\ \mathbf{a}_{r,b} = \mathbf{a}_r + \frac{2h}{3}\mathbf{b}_r \end{cases} \tag{14}$$

Here, the monolayer and bilayer plates are supposed to have the same initial geometry and the same total thickness h.

2.2.3 The Inverse Problem Resolution. In terms of the theory of non-Euclidean plates, the inverse problem consists in determining the rest configuration that leads to a target configuration due to the elastic material response. The rest configuration contains information on the introduced eigenstrains, which, in turn, are caused by the peening treatment. In the bilayer case, solving the inverse problem means finding the rest first fundamental forms of the bottom and top layers $\mathbf{a}_{r,b}$ and $\mathbf{a}_{r,t}$, respectively, as a function of the target shape described by $\mathbf{a}_{\mathrm{tar}}$ and $\mathbf{b}_{\mathrm{tar}}$. As each fundamental form is represented by a symmetric 2×2 matrix, the target configuration is locally defined by six scalar fields over domain U: a_{tar}^{xx}, a_{tar}^{xy}, a_{tar}^{yy} and b_{tar}^{xx}, b_{tar}^{xy}, b_{tar}^{yy}. At the same time, the rest configuration has six degrees-of-freedom: $a_{r,b}^{xx}$, $a_{r,b}^{xy}$, $a_{r,b}^{yy}$ and $a_{r,t}^{xx}$, $a_{r,t}^{xy}$, $a_{r,t}^{yy}$. In the general case, assigning independent values to all six degrees-of-freedom means inducing local *orthotropic* eigenstrain, so that $\varepsilon_{11}(x, y, z) \neq \varepsilon_{22}(x, y, z)$, where ε_{11} and ε_{22} are the local principal eigenstrains. Such local control over the principal eigenstrains is generally not possible with shot peen forming, because here we assume that shot peening induces local *isotropic* in-plane strain. Thus, at each point we only control two degrees-of-freedom: $\varepsilon^t(x, y)$ and $\varepsilon^b(x, y)$. Hence, we have control over fewer

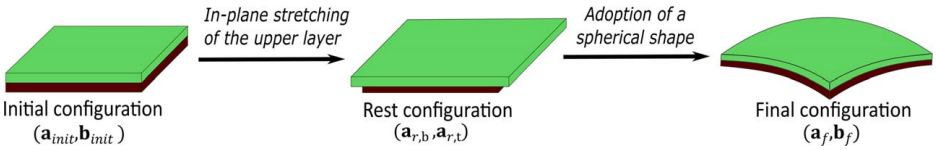

Fig. 4 An example of geometric incompatibility in a bilayer plate inspired by van Rees et al. [19]. The initial configuration described by the fundamental forms ($\mathbf{a}_{init}$, $\mathbf{b}_{init}$) is a flat unstretched rectangular plate, so that $\mathbf{a}_{init}$ is the identity matrix and $\mathbf{b}_{init}$ is the zero matrix along the whole surface. The rest configuration ($\mathbf{a}_{r,t}$, $\mathbf{a}_{r,b}$) prescribes isotropic in-plane stretching of the top layer and shrinking of the bottom layer while conserving the flat shape, so that $\mathbf{a}_{r,t} \neq \mathbf{a}_{init}$, $\mathbf{a}_{r,b} \neq \mathbf{a}_{init}$, $\mathbf{b}_{r,t} = \mathbf{b}_{init}$, and $\mathbf{b}_{r,b} = \mathbf{b}_{init}$. Since peen forming causes in-plane eigenstrain, we do not consider cases when $\mathbf{b}_{r,t} \neq 0$ and $\mathbf{b}_{r,b} \neq 0$ for our simulations, so that the rest configuration is entirely described by ($\mathbf{a}_{r,t}$, $\mathbf{a}_{r,b}$). Adoption of the rest configuration means dissection of the plate in two layers. Instead, the plate adopts an integral but residually stressed final configuration ($\mathbf{a}_f$, $\mathbf{b}_f$) described by compatible fundamental forms.

degrees-of-freedom than input variables. In this case, a solution leading exactly to the target shape may not exist, so we can only numerically optimize $\mathbf{a}_{r,t}$ and $\mathbf{a}_{r,b}$. The uniqueness of solution is not guaranteed either.

3 Methodology

Our method for the inverse problem resolution consists in the iterative correction of the peening pattern on a local scale until convergence is reached within a tolerance and subsequent grouping of the pattern. The grouping algorithm divides the pattern in zones treated with predefined peening regimes.

3.1 Iterative Adjustment of the Peening Pattern. The iterative method idea is to adjust the rest configuration by comparing the local stretching and curvature of the current shape with the stretching and curvature of the target shape. The current shape is computed at each iteration through a numerical resolution of the forward problem. For the initial guess, we use analytical expressions to approximately define an appropriate rest configuration.

3.1.1 The Initial Guess. We characterize the target configuration in terms of fundamental forms ($\mathbf{a}_{tar}$, $\mathbf{b}_{tar}$). Let us consider the monolayer rest configuration $\left(\mathbf{a}_r^{ortho}, \mathbf{b}_r^{ortho}\right)$ described by $\mathbf{a}_r^{ortho} = \mathbf{a}_{tar}$ and $\mathbf{b}_r^{ortho} = \mathbf{b}_{tar}$, that in a general case prescribes local orthotropic in-plane strain. According to the expression for the elastic energy (Eq. (10)), imposition of this rest configuration makes the plate adopt exactly the target configuration, which minimizes the elastic energy. Following Ref. [19], we express the equivalent bilayer rest configuration $\left(\mathbf{a}_{r,t}^{ortho}, \mathbf{a}_{r,b}^{ortho}\right)$ using Eq. (14):

$$\begin{cases} \mathbf{a}_{r,t}^{ortho} = \mathbf{a}_r^{ortho} - \frac{2h}{3}\mathbf{b}_r^{ortho} \\ \mathbf{a}_{r,b}^{ortho} = \mathbf{a}_r^{ortho} + \frac{2h}{3}\mathbf{b}_r^{ortho} \end{cases} \tag{15}$$

Equivalently, using the definition of $\left(\mathbf{a}_r^{ortho}, \mathbf{b}_r^{ortho}\right)$, we rewrite

$$\begin{cases} \mathbf{a}_{r,t}^{ortho} = \mathbf{a}_{tar} - \frac{2h}{3}\mathbf{b}_{tar} \\ \mathbf{a}_{r,b}^{ortho} = \mathbf{a}_{tar} + \frac{2h}{3}\mathbf{b}_{tar} \end{cases} \tag{16}$$

Thus, application of the rest configuration $\left(\mathbf{a}_{r,t}^{ortho}, \mathbf{a}_{r,b}^{ortho}\right)$ leads to the target shape ($\mathbf{a}_{tar}$, $\mathbf{b}_{tar}$). However, this configuration implies local orthotropic eigenstrain, which is not feasible with shot peen forming. We comply with this constraint and find a suitable local isotropic eigenstrain based on this prediction. To that end, we first compute the local eigenstrains in the principal directions in the top (ε_{11}^t, ε_{22}^t) and bottom (ε_{11}^b, ε_{22}^b) layers of the bilayer prescribed by $\mathbf{a}_{r,t}^{ortho}$ and $\mathbf{a}_{r,b}^{ortho}$, respectively. Next, we take their averages ε_{avg}^t and ε_{avg}^b and impose them locally in all in-plane directions thus making the initial guess.

To find (ε_{11}^t, ε_{22}^t) and (ε_{11}^b, ε_{22}^b), we perform a spectral decomposition of $\mathbf{a}_{r,t}^{ortho}$ and $\mathbf{a}_{r,b}^{ortho}$, respectively [19]. At the top layer, the distortions prescribed by $\mathbf{a}_{r,t}^{ortho}$ imply stretching by a factor of $(\varepsilon_{11}^t + 1)$ in the first principal direction and by a factor of $(\varepsilon_{22}^t + 1)$ in the orthogonal second principal direction. The first principal direction is rotated by an angle of θ^t with respect to the x-axis. At the bottom layer, the stretch factors are $(\varepsilon_{11}^b + 1)$ and $(\varepsilon_{22}^b + 1)$, and the first principal direction is rotated by an angle of θ^b with respect to the x-axis. The initial configuration is unstretched, so its first fundamental form $\mathbf{a}_{init}$ is represented by the identity matrix:

$$\mathbf{a}_{init} = \mathbf{I} \tag{17}$$

Consequently, the eigenvalues of $\mathbf{a}_t^{ortho}$ equal $(\varepsilon_{11}^t + 1)^2$ and $(\varepsilon_{22}^t + 1)^2$, and the eigenvalues of $\mathbf{a}_b^{ortho}$ equal $(\varepsilon_{11}^b + 1)^2$ and $(\varepsilon_{22}^b + 1)^2$, so that

$$\mathbf{a}_{r,j}^{ortho} = \begin{bmatrix} \cos(\theta^j) & -\sin(\theta^j) \\ \sin(\theta^j) & \cos(\theta^j) \end{bmatrix}^T \begin{bmatrix} (\varepsilon_{11}^j + 1)^2 & 0 \\ 0 & (\varepsilon_{22}^j + 1)^2 \end{bmatrix} \begin{bmatrix} \cos(\theta^j) & -\sin(\theta^j) \\ \sin(\theta^j) & \cos(\theta^j) \end{bmatrix} \quad \text{for } j = t, b \tag{18}$$

We deduce the local eigenstrain in the principal directions (ε_{11}^t, ε_{22}^t) and (ε_{11}^b, ε_{22}^b) from the eigenvalues and calculate the average local eigenstrain ε_{avg}^t and ε_{avg}^b for both layers:

$$\varepsilon_{avg}^j = \frac{\varepsilon_{11}^j + \varepsilon_{22}^j}{2} \quad \text{for } j = t, b \tag{19}$$

We impose the local isotropic eigenstrain ε_{avg}^t and ε_{avg}^b on the top and bottom layers, respectively, thus making the initial guess. The bilayer rest fundamental forms $\mathbf{a}_{r,t}$ and $\mathbf{a}_{r,b}$ corresponding to this strain are expressed as

$$\mathbf{a}_{r,j} = \begin{bmatrix} (\varepsilon_{avg}^j + 1)^2 & 0 \\ 0 & (\varepsilon_{avg}^j + 1)^2 \end{bmatrix} \quad \text{for } j = t, b \tag{20}$$

We substitute ($\mathbf{a}_{r,t}$, $\mathbf{a}_{r,b}$) to the bilayer elastic energy functional (Eq. (12)) and find the *current* shape ($\mathbf{a}_c$, $\mathbf{b}_c$) through numerical minimization of the functional.

Following Eq. (13), it is possible to find equivalent monolayer rest fundamental forms ($\mathbf{a}_r$, $\mathbf{b}_r$). Prescription of the rest fundamental forms ($\mathbf{a}_r$, $\mathbf{b}_r$) to a monolayer plate leads to the same current shape ($\mathbf{a}_c$, $\mathbf{b}_c$) as the prescription of ($\mathbf{a}_{r,t}$, $\mathbf{a}_{r,b}$) to a bilayer plate. Essentially, ($\mathbf{a}_r$, $\mathbf{b}_r$) can be viewed as the rest configuration imposed on the bilayer mid-surface. The forms $\mathbf{a}_r$ and $\mathbf{b}_r$ may be incompatible as they were defined analytically, but $\mathbf{a}_c$ and $\mathbf{b}_c$ are always compatible because they describe a surface in Euclidean space. Consequently, ($\mathbf{a}_c$, $\mathbf{b}_c$) are typically different from ($\mathbf{a}_r$, $\mathbf{b}_r$).

3.1.2 Adjustment of the Local Stretching. In the previous section, we defined a procedure to obtain a quick estimate of the inverse problem by solving for orthotropic expansions and averaging them to estimate isotropic expansions. In this section and the next, we seek to iteratively correct these expansions using only local information.

As the rest configuration ($\mathbf{a}_{r,t}$, $\mathbf{a}_{r,b}$) prescribes local *isotropic* in-plane strain, we measure stretching in terms of local areas. The area A of each region of the surface constrained by $(x, y) \in U_1 \subset \mathbb{R}^2$ is expressed in terms of the first fundamental form $\mathbf{a}$ as $A = \iint_{U_1} \sqrt{\det(\mathbf{a})}\, dxdy$. The first fundamental form is considered constant inside small regions, so we conclude that the current area of each small region A_c and its target area A_{tar} are related as

$$\frac{A_{\text{tar}}}{A_c} \approx \frac{\sqrt{\det(\mathbf{a}_{\text{tar}})}}{\sqrt{\det(\mathbf{a}_c)}} = k_A \tag{21}$$

This means that if we locally multiply $\mathbf{a}_c$ by the coefficient k_A, then the current area will equal that of the target. However, we are only able to influence $\mathbf{a}_c$ indirectly through the adjustment of $\mathbf{a}_r$. Consequently, as a part of the iterative procedure, we multiply $\mathbf{a}_r$ by k_A and thus obtain the equivalent monolayer rest fundamental form $\mathbf{a}_r^{\text{new}}$ to be imposed during the subsequent iteration:

$$\mathbf{a}_r^{\text{new}} = k_A \mathbf{a}_r \tag{22}$$

The $\mathbf{a}_r^{\text{new}}$ may be different from the current first fundamental form on the subsequent iteration $\mathbf{a}_c^{\text{new}}$, and thus this correction of the rest fundamental form does not lead to an exact solution but allows to approach it. In other words, multiplication of $\mathbf{a}_r$ by k_A does not correct the local area exactly by the coefficient k_A but reduces the difference between the current local stretching and the target one.

3.1.3 Adjustment of the Local Curvature. We characterize the surface curvature in terms of the local mean curvature H. By definition, H is the average of two local principal curvatures κ_1 and κ_2 that are computed as eigenvalues of the shape operator $\mathbf{S} = \mathbf{a}^{-1}\mathbf{b}$ [26]. We compute the local ratios k_H between the current mean curvatures H_c and the target mean curvatures H_{tar} and assign an upper threshold δ for $|k_H|$:

$$\begin{cases} k_H = \frac{H_{\text{tar}}}{H_c} & \text{for } \left|\frac{H_{\text{tar}}}{H_c}\right| < \delta \\ k_H = \delta \cdot sgn\left(\frac{H_{\text{tar}}}{H_c}\right) & \text{for } \left|\frac{H_{\text{tar}}}{H_c}\right| \geq \delta \end{cases} \tag{23}$$

Here, H_{tar} is the average of the two eigenvalues of $\mathbf{S}_{\text{tar}} = \mathbf{a}_{\text{tar}}^{-1}\mathbf{b}_{\text{tar}}$, and H_c is the average of the two eigenvalues of $\mathbf{S}_c = \mathbf{a}_c^{-1}\mathbf{b}_c$. The threshold δ is assigned in order to deal with special cases when $|H_c|$ is small. Provided that multiplication of a matrix by a constant multiplies its eigenvalues by the same constant, the multiplication of $\mathbf{S}_c$ by k_H would make the current local mean curvatures equal to those of the target. As we are unable to adjust any of the current fundamental forms ($\mathbf{a}_c$, $\mathbf{b}_c$) directly, we influence them through adjustment of the rest fundamental forms ($\mathbf{a}_r$, $\mathbf{b}_r$) in order to get

$$\mathbf{S}_r^{\text{new}} = k_H \mathbf{S}_r = k_H \mathbf{a}_r^{-1}\mathbf{b}_r = k_H k_A \frac{\mathbf{a}_r^{-1}}{k_A}\mathbf{b}_r = k_H k_A \left(\mathbf{a}_r^{\text{new}}\right)^{-1}\mathbf{b}_r \tag{24}$$

Thus, we define

$$\mathbf{b}_r^{\text{new}} = k_H k_A \mathbf{b}_r \tag{25}$$

Once the $\mathbf{a}_r^{\text{new}}$ and $\mathbf{b}_r^{\text{new}}$ are found, we compute the bilayer rest fundamental forms ($\mathbf{a}_{r,t}^{\text{new}}$, $\mathbf{a}_{r,b}^{\text{new}}$) as

$$\begin{cases} \mathbf{a}_{r,t}^{\text{new}} = \mathbf{a}_r^{\text{new}} - \frac{2h}{3}\mathbf{b}_r^{\text{new}} \\ \mathbf{a}_{r,b}^{\text{new}} = \mathbf{a}_r^{\text{new}} + \frac{2h}{3}\mathbf{b}_r^{\text{new}} \end{cases} \tag{26}$$

Next, we substitute ($\mathbf{a}_{r,t}^{\text{new}}$, $\mathbf{a}_{r,b}^{\text{new}}$) to the bilayer elastic energy functional (Eq. (12)) and find the current shape ($\mathbf{a}_c^{\text{new}}$, $\mathbf{b}_c^{\text{new}}$) that minimizes the elastic energy.

3.1.4 Subsequent Iterations and Stop Criterion. We compare the current shape with the target shape and recalculate the bilayer rest fundamental forms until a convergence criterion is satisfied. The convergence criterion is based on the calculation of the Hausdorff distance d_H between the new current configuration $\mathcal{C}_c^{\text{new}}$ defined by ($\mathbf{a}_c^{\text{new}}$, $\mathbf{b}_c^{\text{new}}$) and the current configuration from the previous iteration $\mathcal{C}_c$ defined by ($\mathbf{a}_c$, $\mathbf{b}_c$). We nondimensionalize d_H by the square root of the total area of the plate in its initial configuration A_{total}. We stop iterating either when a predefined maximal number of iterations M is reached, or when the nondimensionalized Hausdorff distance becomes inferior to a chosen threshold τ:

$$\frac{d_H(\mathcal{C}_c, \mathcal{C}_c^{\text{new}})}{\sqrt{A_{\text{total}}}} < \tau \tag{27}$$

3.1.5 Calculation of the Adjusted Eigenstrain. We denote the bilayer *final rest* fundamental forms, i.e., the ones obtained on the last iteration, as ($\mathbf{a}_{rf,t}$, $\mathbf{a}_{rf,b}$). To relate them with peen forming parameters, we determine the recalculated eigenstrain ($\varepsilon^{rf,t}$, $\varepsilon^{rf,b}$).

Provided that the iterative adjustment implies only addition, subtraction, and multiplication by a constant of diagonal matrices, the $\mathbf{a}_{rf,t}$ and $\mathbf{a}_{rf,b}$ are diagonal. Moreover, the imposed local eigenstrain ($\varepsilon^{rf,t}$, $\varepsilon^{rf,b}$) is isotropic, so $\mathbf{a}_{rf,t}$ and $\mathbf{a}_{rf,b}$ have the following form:

$$\mathbf{a}_{rf,j} = \begin{bmatrix} \left(\varepsilon^{rf,j}+1\right)^2 & 0 \\ 0 & \left(\varepsilon^{rf,j}+1\right)^2 \end{bmatrix} \quad \text{for } j = t, b \tag{28}$$

Consequently,

$$\varepsilon^{rf,j} = \sqrt{a_{rf,j}^{11}} - 1 \quad \text{for } j = t, b \tag{29}$$

3.2 Numerical Implementation. We mesh the plate midsurface with triangular elements and follow the energy calculation strategy presented in Refs. [17,27]. The first and the second fundamental forms are estimated separately for each element and are constant inside the element. The global elastic energy is calculated as a sum of local energetical contributions from all the elements.

The first fundamental form on a triangular element such as that schematized in Fig. 5 depends entirely on the coordinates of the vertices. The three vertices are defined by position vectors $\vec{v}_0$, $\vec{v}_1$, and $\vec{v}_2$, and the edge vectors constituting the triangle are expressed as: $\vec{e}_0 = \vec{v}_1 - \vec{v}_0$, $\vec{e}_1 = \vec{v}_2 - \vec{v}_1$, and $\vec{e}_2 = \vec{v}_0 - \vec{v}_2$. These vectors are tangent to the plane containing the triangle, so following Eq. (8), the first fundamental form on a triangular element is computed as

$$\mathbf{a} = \begin{bmatrix} \vec{e}_1 \cdot \vec{e}_1 & \vec{e}_1 \cdot \vec{e}_2 \\ \vec{e}_2 \cdot \vec{e}_1 & \vec{e}_2 \cdot \vec{e}_2 \end{bmatrix} \tag{30}$$

In a general case of isotropic eigenstrain ε^r imposed on a triangular element, its rest first fundamental form $\mathbf{a}_r$ is expressed as

$$\begin{aligned} \mathbf{a}_r &= \begin{bmatrix} \vec{e}_1^{\text{init}} \cdot \vec{e}_1^{\text{init}} & \vec{e}_1^{\text{init}} \cdot \vec{e}_2^{\text{init}} \\ \vec{e}_2^{\text{init}} \cdot \vec{e}_1^{\text{init}} & \vec{e}_2^{\text{init}} \cdot \vec{e}_2^{\text{init}} \end{bmatrix} \begin{bmatrix} (\varepsilon^r+1)^2 & 0 \\ 0 & (\varepsilon^r+1)^2 \end{bmatrix} \\ &= \mathbf{a}_{\text{init}} \begin{bmatrix} (\varepsilon^r+1)^2 & 0 \\ 0 & (\varepsilon^r+1)^2 \end{bmatrix} \end{aligned} \tag{31}$$

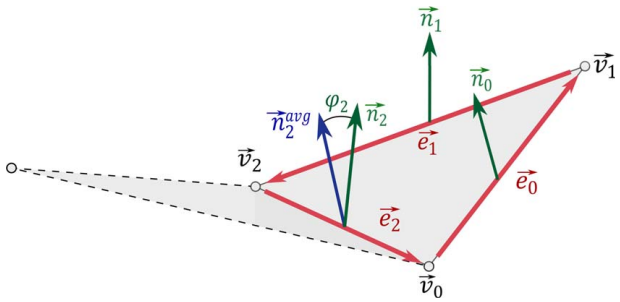

Fig. 5 A triangular mesh element and vectors that determine local fundamental forms: the vertex position vectors ($\vec{v}_0$, $\vec{v}_1$, and $\vec{v}_2$), the edge vectors ($\vec{e}_0$, $\vec{e}_1$, and $\vec{e}_2$), and the mid-edge normals ($\vec{n}_0$, $\vec{n}_1$, and $\vec{n}_2$). The mid-edge normals are perpendicular to the edge, and their direction is determined by the angle of inclination with respect to the average normal of the two adjacent faces. Thus, the direction of $\vec{n}_2$ is determined by the angle φ_2. This angle is measured with respect to $\vec{n}_{\text{avg}}$, which is the average normal of the two faces that share the edge $\vec{e}_2$.

where $\vec{e}_1^{\,\text{init}}$, $\vec{e}_2^{\,\text{init}}$, and $\vec{e}_3^{\,\text{init}}$ are the edge vectors in the initial configuration and $\mathbf{a}_{\text{init}}$ is the element first fundamental form in its initial configuration. Otherwise, if an orthotropic in-plane strain is imposed, then the rest first fundamental form $\mathbf{a}_r^{\text{ortho}}$ becomes

$$\mathbf{a}_r^{\text{ortho}} = \mathbf{a}_{\text{init}} \begin{bmatrix} \cos(\theta) & -\sin(\theta) \\ \sin(\theta) & \cos(\theta) \end{bmatrix}^T \begin{bmatrix} (\varepsilon_{11}^r + 1)^2 & 0 \\ 0 & (\varepsilon_{22}^r + 1)^2 \end{bmatrix} \times \begin{bmatrix} \cos(\theta) & -\sin(\theta) \\ \sin(\theta) & \cos(\theta) \end{bmatrix} \tag{32}$$

where ε_{11}^r and ε_{22}^r define the eigenstrain imposed in the principal directions and θ stands for the angle between the first principal direction and the x axis.

The second fundamental form defines the surface curvature, so the information about surface normals is required. In this connection, we introduce a unit normal vector $\vec{n}_i$, $i = 1, 2, 3$, at the center of each edge of the mesh (the *edge-director*). This vector is normal to the edge, and its angle of inclination φ_i, $i = 1, 2, 3$, in the plane perpendicular to the edge provides a supplementary degree-of-freedom. This angle is measured with respect to the average of the adjacent face normals [27]. A finite-difference approximation of the derivatives appearing in Eq. (9) yields the following expression for the second fundamental form of a triangular element:

$$\mathbf{b} = \begin{bmatrix} \vec{e}_1 \cdot 2(\vec{n}_0 - \vec{n}_2) & \vec{e}_1 \cdot 2(\vec{n}_1 - \vec{n}_0) \\ \vec{e}_1 \cdot 2(\vec{n}_1 - \vec{n}_0) & \vec{e}_2 \cdot 2(\vec{n}_1 - \vec{n}_0) \end{bmatrix} = \begin{bmatrix} \vec{e}_1 \cdot 2(\vec{n}_0 - \vec{n}_2) & -\vec{e}_1 \cdot \vec{n}_0 \\ -\vec{e}_1 \cdot \vec{n}_0 & \vec{e}_2 \cdot 2(\vec{n}_1 - \vec{n}_0) \end{bmatrix} \tag{33}$$

According to Eq. (12), the global elastic energy for a plate composed of K triangular elements is expressed in terms of local fundamental forms as

$$\begin{aligned} E_{\text{BL}} = \frac{1}{2}\sum_{k=1}^{K} \Bigg[& \frac{h_k}{8} \left\| (\mathbf{a}_{r,b}^{-1})_k (\mathbf{a}_f)_k - \mathbf{I} \right\|_e^2 + \frac{(h_k)^3}{24} \left\| (\mathbf{a}_{r,b}^{-1})_k (\mathbf{b}_f)_k \right\|_e^2 \\ & + \frac{(h_k)^2}{8} \left\langle \left((\mathbf{a}_{r,b}^{-1})_k (\mathbf{a}_f)_k - \mathbf{I} \right), (\mathbf{a}_{r,b}^{-1})_k (\mathbf{b}_f)_k \right\rangle_e \Bigg] \sqrt{\det(\mathbf{a}_{r,b})_k} \\ & + \frac{1}{2}\sum_{k=1}^{K} \Bigg[\frac{h_k}{8} \left\| (\mathbf{a}_{r,t}^{-1})_k (\mathbf{a}_f)_k - \mathbf{I} \right\|_e^2 + \frac{(h_k)^3}{24} \left\| (\mathbf{a}_{r,t}^{-1})_k (\mathbf{b}_f)_k \right\|_e^2 \\ & - \frac{(h_k)^2}{8} \left\langle \left((\mathbf{a}_{r,t}^{-1})_k (\mathbf{a}_f)_k - \mathbf{I} \right), (\mathbf{a}_{r,t}^{-1})_k (\mathbf{b}_f)_k \right\rangle_e \Bigg] \sqrt{\det(\mathbf{a}_{r,t})_k} \end{aligned} \tag{34}$$

The local plate thickness h_k can be different for each element. Similarly, the local Young's modulus Y_k and the Poisson's ratio ν_k can vary along the plate.

As follows from Eq. (31), the element's rest first fundamental forms $\mathbf{a}_{r,t}$ and $\mathbf{a}_{r,b}$ for the isotropic growth case are defined by the imposed local eigenstrain ε^t and ε^b and the initial vertex positions $\vec{v}_i^{\,\text{init}}$, $i = 1, 2, 3$. At the same time, according to Eqs. (30) and (33), the two final fundamental forms $\mathbf{a}_f$ and $\mathbf{b}_f$ are defined by the final vertex positions $\vec{v}_i^{\,f}$, $i = 1, 2, 3$, and final angles of inclination of the edge directors φ_i^f, $i = 1, 2, 3$. Numerically, the forward problem consists in minimizing the global elastic energy functional equation (34) with respect to $\vec{v}_i^{\,f}$ and φ_i^f provided with $\vec{v}_i^{\,\text{init}}$, ε^t, and ε^b. We perform the minimization using a quasi-Newton limited-memory Broyden–Fletcher–Goldfarb–Shanno (L-BFGS) algorithm [28]. The gradients of the elastic energy functional required by the minimization algorithm are computed analytically following Ref. [29]. The corresponding programming code for the forward problem resolution was developed by van Rees and is publicly accessible [30].

In this implementation, the inverse problem resolution consists in finding the local eigenstrain $\varepsilon^{rf,t}$ and $\varepsilon^{rf,b}$ to be imposed on each triangular element. This means that the iterative correction of the rest fundamental forms $\mathbf{a}_{r,t}$ and $\mathbf{a}_{r,b}$ is executed on a local scale for each element separately, while the forward problem is resolved on each iteration on a global scale, thus reflecting the mechanics of the plate.

3.3 Grouping of the Peening Pattern. In the general case, the eigenstrains ($\varepsilon^{rf,t}$, $\varepsilon^{rf,b}$) provided by Algorithm 1 are different for each element and can take any real values. Peen forming often deals with smoothly curved target shapes, so ($\varepsilon^{rf,t}$, $\varepsilon^{rf,b}$) may also vary smoothly along the surface given that these two values depend on the target shape curvature. We call the eigenstrain pattern provided by the Algorithm 1 the *free* pattern. From a practical point of view, each pair ($\varepsilon^{rf,t}$, $\varepsilon^{rf,b}$) represents a peening regime. However, a limited number of regimes is available when peening a real part. Thus, we divide the pattern into zones with uniform prescribed eigenstrain and obtain a *grouped* pattern.

Algorithm 1 The inverse problem resolution

The iterative loop

while condition (27) is not satisfied and the number of iterations is below maximum **do**
  for each triangular element
    Find principal curvatures (κ_1^c, κ_2^c) as eigenvalues of the shape operator $\mathbf{S}_c = \mathbf{a}_c^{-1}\,\mathbf{b}_c$
    Compute the current mean curvature as $H_c = 0.5(\kappa_1^c + \kappa_2^c)$
    Compute the current area as $A_c = \sqrt{\det(\mathbf{a}_c)}$
    Compute the ratios k_A and k_H following Eqs. (21) and (23), respectively
    Compute the monolayer rest fundamental forms $\mathbf{a}_r$ and $\mathbf{b}_r$ following Eq. (13) using only local information
    Compute the adjusted monolayer rest fundamental forms $\mathbf{a}_r^{\text{new}}$ and $\mathbf{b}_r^{\text{new}}$ a following Eqs. (22) and (25), respectively
    Compute the adjusted bilayer rest fundamental forms $\mathbf{a}_{r,t}^{\text{new}}$ and $\mathbf{a}_{r,b}^{\text{new}}$ following Eq. (26)
  end for
  Substitute $\mathbf{a}_{r,t}^{\text{new}}$ and $\mathbf{a}_{r,b}^{\text{new}}$ to the bilayer elastic energy functional (Eq. (34)) and minimize it to solve the forward problem and find the current configuration ($\mathbf{a}_c^{\text{new}}$, $\mathbf{b}_c^{\text{new}}$)
end while

The initial guess

for each triangular element
  Compute the first fundamental form of the initial shape $\mathbf{a}_{\text{init}}$ following Eq. (30)
  Compute the monolayer fundamental forms of the target shape $\mathbf{a}_{\text{tar}}$ and $\mathbf{b}_{\text{tar}}$ following Eqs. (30) and (33), respectively
  Find principal curvatures k_2^{tar} and k_1^{tar} as eigenvalues of the target shape operator $\mathbf{S}_{\text{tar}} = \mathbf{a}_{\text{tar}}^{-1}\mathbf{b}_{\text{tar}}$
  Compute the target mean curvature as $H_{\text{tar}} = 0.5(\kappa_1^{\text{tar}} + \kappa_2^{\text{tar}})$
  Compute the target area as $A_{\text{tar}} = \sqrt{\det(\mathbf{a}_{\text{tar}})}$
  Compute the orthotropic bilayer rest fundamental forms $\mathbf{a}_{r,t}^{\text{ortho}}$ and $\mathbf{a}_{r,b}^{\text{ortho}}$ following Eq. (16)
  Find eigenvalues λ_1^j and λ_2^j of $(\mathbf{a}_{\text{init}}^{-1}\mathbf{a}_{r,j}^{\text{ortho}})$ for $j = t, b$
  Compute the orthotropic eigenstrain as $\varepsilon_{ii}^j = \sqrt{\lambda_i^j} - 1$ for $i = 1, 2$ and $j = t, b$
  Compute the average eigenstrain $\varepsilon_{\text{avg}}^t$ and $\varepsilon_{\text{avg}}^b$ following Eq. (19)
  Compute bilayer rest fundamental forms $\mathbf{a}_{r,t}$ and $\mathbf{a}_{r,b}$ by substituting $\varepsilon_{\text{avg}}^t$ and $\varepsilon_{\text{avg}}^b$, respectively, for år in Eq. (31)
end for
Substitute $\mathbf{a}_{r,t}$ and $\mathbf{a}_{r,b}$ to the bilayer elastic energy functional (Eq.(34)) and minimize it to solve the forward problem and find the current configuration (a_c, b_c)

Final step after exiting the iterative loop

for each triangular element **do**
  Compute the eigenstrain $\varepsilon^{rf,t}$ and $\varepsilon^{rf,b}$ prescribed by $\mathbf{a}_{rf,t} = \mathbf{a}_{r,t}^{\text{new}}$ and by $\mathbf{a}_{rf,b} = \mathbf{a}_{r,b}^{\text{new}}$, respectively, following Eq. (29)
end for

We associate all triangular elements with points on a plane with cartesian coordinates (ε^t, ε^b), and the coordinates of each point k are

determined by the eigenstrain $\left(\varepsilon_k^{rf,t}, \varepsilon_k^{rf,b}\right)$ assigned to the corresponding element k, as illustrated in Fig. 6. We divide the points in groups, and the group centroids are determined by the predefined peening regimes. We denote the centroid of a group n by $\left(\varepsilon_n^{\text{cen},t}, \varepsilon_n^{\text{cen},b}\right)$. Each point $\left(\varepsilon_k^{rf,t}, \varepsilon_k^{rf,b}\right)$ is attributed to the group with the closest centroid in terms of Euclidean distance. When all points are grouped, we homogenize the eigenstrain inside each group, i.e., we assign the eigenstrain $\left(\varepsilon_n^{\text{cen},t}, \varepsilon_n^{\text{cen},b}\right)$ to all triangular elements that fall into the group n.

Consider N predefined peening regimes such as the ones illustrated in Fig. 7. Regime $i = 1, 2, \ldots, N$ induces expansions ε_i^t and ε_i^b on the treated and opposite layers, respectively. In addition, we consider the lack of treatment $\varepsilon_0^t = \varepsilon_0^b = 0$. Since the top and bottom surfaces can be peened independently, there are $(N+1)^2$ possible treatment combinations. Each treatment combination gives rise to a group centroid. Combining regime $i = 1, 2, \ldots, N$ on the top surface with regime $j = 1, 2, \ldots, N$ on the bottom surface leads to the following expansions of the top and bottom surfaces: $(\varepsilon_i^t, \varepsilon_i^b) + (\varepsilon_j^t, \varepsilon_j^b) = (\varepsilon_{ij}^{\text{cen},t}, \varepsilon_{ij}^{\text{cen},b})$. Figure 7 illustrates this principle. Figure 6(*e*) also provides a cartesian representation of $(N+1)^2$ centroids for the case $N = 1$.

3.4 Numerical Validation of the Inverse Problem Solver. We generated target shapes numerically to test our algorithms for the iterative inverse problem resolution and grouping. To ensure that the target shapes were achievable with peen forming, we generated them by assigning a random peening pattern to the initial configuration and then solved the forward problem. The random peening patterns were generated following Algorithm 2.

Algorithm 2 Generation of random peening patterns

```
Mark 1 to 6 random points on the top and bottom surfaces of the plate
for each point do
    Draw a square of random size (but not bigger than the plate size) centered on the point
    Assign randomly one of the available peening regimes to the square
    if the square protrudes beyond the plate area then
        Translate the part that protrudes symmetrically on the other side of the plate
    end if
    if the square superimposes with a previously drawn square on the same side then
        Erase the previously assigned regime in the superimposing area and leave only the latest one
    end if
end for
```

When the target shapes were generated, we solved the inverse problem for each of them following Algorithm 1 and then grouped the peening pattern. The predefined regimes were fixed as those that were originally used to generate the target shapes. To quantify the error, we solved the forward problem for the free and the grouped patterns. We thus obtained two final shapes for

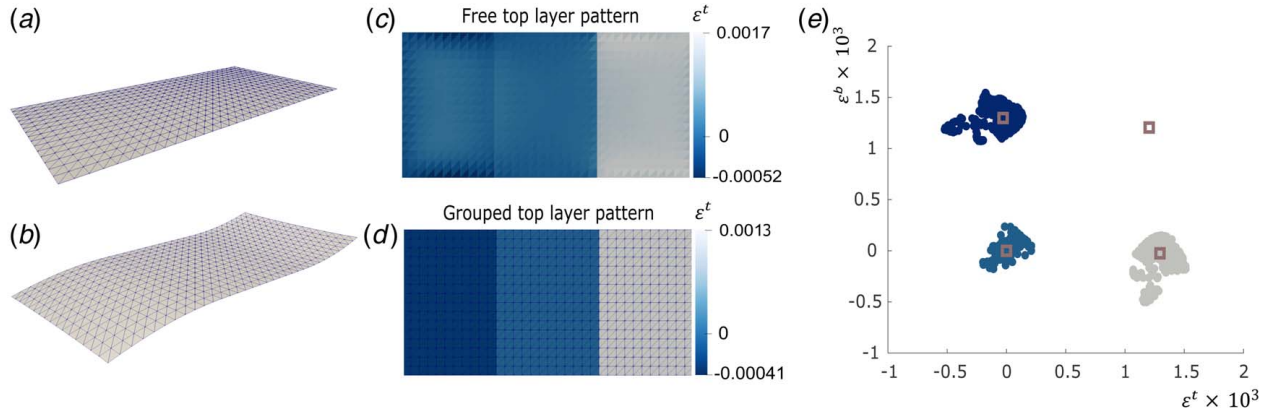

Fig. 6 Graphical representation of grouping of the eigenstrain pattern. The triangulated flat initial configuration, (*a*) and the target configuration—wavy shape, (*b*)—are the input data for the inverse problem resolution. We divide the eigenstrain pattern, (c) into three zones treated uniformly. (*d*) A plane with cartesian coordinates (ε^t, ε^b), (e) illustrates the grouping from the numerical point of view. The points correspond to the eigenstrain assigned to each element of the triangular mesh. The four centroids are denoted by squares. They are generated by one peening regime and the lack of treatment as an additional regime. The grouping is based on calculation of the least Euclidean distance from the points to the group centroids. In the presented case, there are no points close to the centroid denoting treatment from both sides, so the corresponding group is empty. Once the points are divided into groups, we homogenize the eigenstrain for all the elements attributed to the same group.

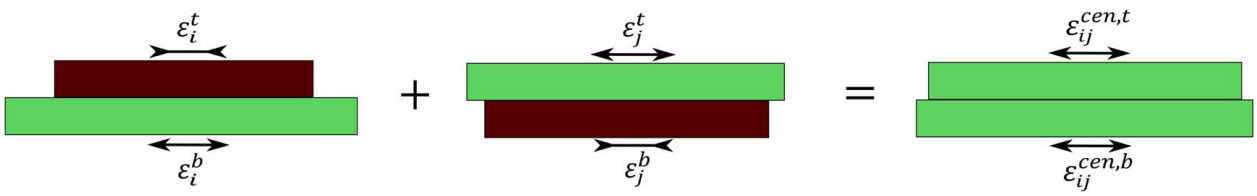

Fig. 7 Calculation of the group centroids. The group *ij* implies treatment from the bottom side with regime *i* and treatment from the top side with regime *j*. Its centroid is determined by a pair of parameters $\varepsilon_{ij}^{\text{cen},t}$ and $\varepsilon_{ij}^{\text{cen},b}$, and each of them is a superposition of eigenstrain generated by the two regimes that form this group: $\varepsilon_{ij}^{\text{cen},t} = \varepsilon_i^t + \varepsilon_j^t$, $\varepsilon_{ij}^{\text{cen},b} = \varepsilon_i^b + \varepsilon_j^b$. In this example, the regime *i* is more intense than the regime *j*, so $\varepsilon_{ij}^{\text{cen},t} < \varepsilon_{ij}^{\text{cen},b}$.

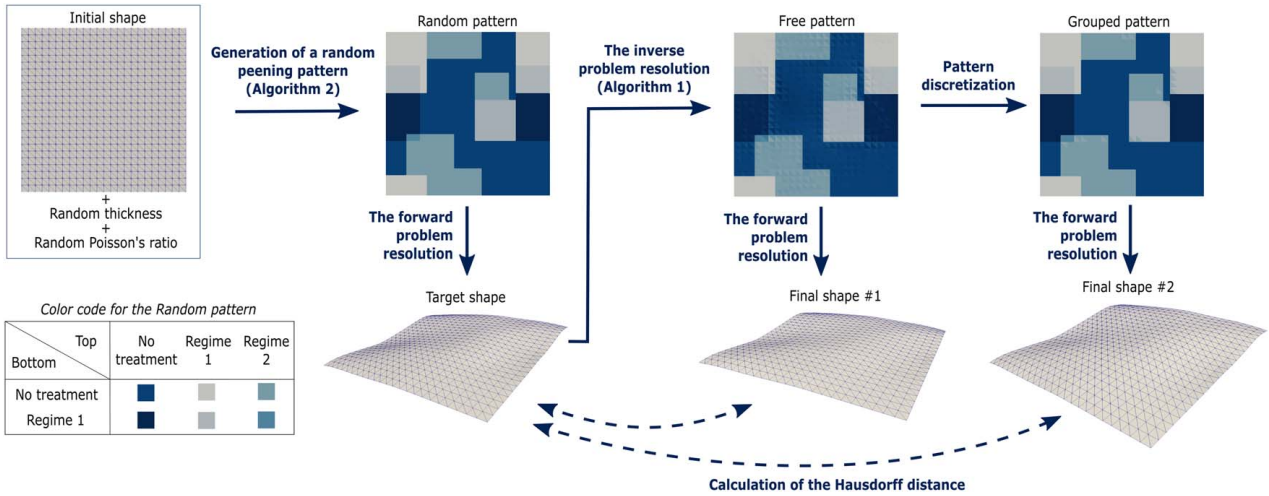

Fig. 8 A validation process to test the quality of the inverse problem resolution. The initial shape is fixed as a flat 1×1 m plate, its thickness and Poisson's ratio are chosen randomly. These parameters are kept constant throughout the whole validation process. A random peening pattern is generated following Algorithm 2 and assigned to the initial shape. We solve the forward problem taking the random pattern as input, and the result is used as the target shape for the inverse problem validation. The eigenstrain pattern is determined following Algorithm 1 and grouped using pre-determined regimes. Finally, the forward problem is resolved for the free and the grouped patterns. The difference between the target shape and the two final shapes is quantified with the nondimensionalized Hausdorff distance Ω.

each test case and compared them with the target shape by calculating the nondimensionalized Hausdorff distance Ω:

$$\Omega = \frac{d_H(\mathcal{C}_f, \mathcal{C}_{\text{tar}})}{\sqrt{A_{\text{total}}}} \tag{35}$$

where $\mathcal{C}_f$ stands for the final configuration and $\mathcal{C}_{\text{tar}}$ stands for the target configuration. The optimal registration of $\mathcal{C}_f$ with respect to $\mathcal{C}_{\text{tar}}$ with the aim of computing $d_H(\mathcal{C}_f, \mathcal{C}_{\text{tar}})$ was done using the iterative closest point algorithm (ICP) [31]. Alternatively, the registration can be done through alignment of several vertices, which are defined for each particular target shape depending on the quality control requirements. The overall process for the inverse problem validation is schematized in Fig. 8.

4 Results

We generated 200 random patterns with Algorithm 2 and applied them on a flat square plate (1 × 1 m). The plate thickness was arbitrarily assigned in each case and ranged from 2 mm to 15 mm. The Poisson's ratio was also arbitrarily picked between 0.32 and 0.36. The value of Young's modulus was set equal to 73 GPa, which is a typical value for 2024 aluminum alloy. The plate was meshed with 1152 triangular elements. The forward problem resolution took 10–30 s for one shape, depending on the pattern and the plate thickness. Thus, the forward problem resolution took longer time for thinner plates with bigger treated areas due to larger deflection of these plates.

For the first 100 test cases (*series 1*), we made only one peening regime available, so the entire treated area was peened with the same parameters. For the second 100 test cases (*series 2*), we assigned randomly one of four available peening regimes to each square on both sides. We considered real peening regimes presented in Ref. [7]. The authors of this paper deduced idealized eigenstrain profiles from the residual stress measurements performed on the treated specimens. The idealized eigenstrain profiles were formulated as one uniformly expanding layer of a constant thickness. The layer thickness and the eigenstrain magnitude were different for each regime. We reformulated the idealized eigenstrain profiles in terms of $(\varepsilon^t, \varepsilon^b)$ by equating the total eigenstrain Γ and the first eigenstrain moment Γ_1 induced by $(\varepsilon^t, \varepsilon^b)$ and by the one expanding layer. Table 1 summarizes the eigenstrain $(\varepsilon^t, \varepsilon^b)$ induced by each of the four regimes applied on a 5 mm thick plate from the top side.

Figures 9 and 10 present the free and the grouped patterns along with the convergence curves for two particular test cases from series 2: a low-error case and a high-error case. Figures 9(*b*) and 10(*b*) show that the free pattern on the final iteration is locally close to the originally generated random pattern. Due to that, most of the elements are grouped correctly, so that the eigenstrains prescribed by the grouped and the random patterns to these elements become equal (Figs. 9(*c*) and 10(*c*)). However, in each case, there are elements that are attributed to a wrong group. In the low-error case, this happens only for several elements. Consequently, the dimensionless error Ω is lower for the grouped pattern than for the free pattern. In the high-error case, the grouped pattern undergoes the *checkerboard* problem, meaning that the pattern locally alternates two peening regimes over a certain area (Fig. 10(*c*)). A large area affected by the checkerboard problem increases the Ω in comparison with the free pattern (Fig. 10(*e*)). Nevertheless, the regimes that are mixed up in the checkerboard-affected zone have only a slight difference in terms of the induced eigenstrain, so the Ω increases up to 0.23% at most.

In terms of convergence, the most important correction is done on the first iteration after the initial guess, as illustrated by Figs. 9(*e*) and 10(*e*). Thus, the first iteration decreases the Ω by 65% on average. All the subsequent iterations together decrease the Ω obtained on the first iteration by 60% on average. Because of the local and simultaneous nature of the eigenstrain adjustment, the

Table 1 The in-plane eigenstrain induced by the regimes used to generate the random peening patterns

Regime	$\varepsilon^t \times 10^3$	$\varepsilon^b \times 10^3$
1	2.5	−0.4
2	3.2	−0.6
3	1.7	−0.4
4	2.0	−0.4

Notes: The in-plane eigenstrain is presented for the case of a 5 mm thick plate. The peening regimes represent four real treatments inducing different eigenstrain profiles, which are examined in Ref. [7].

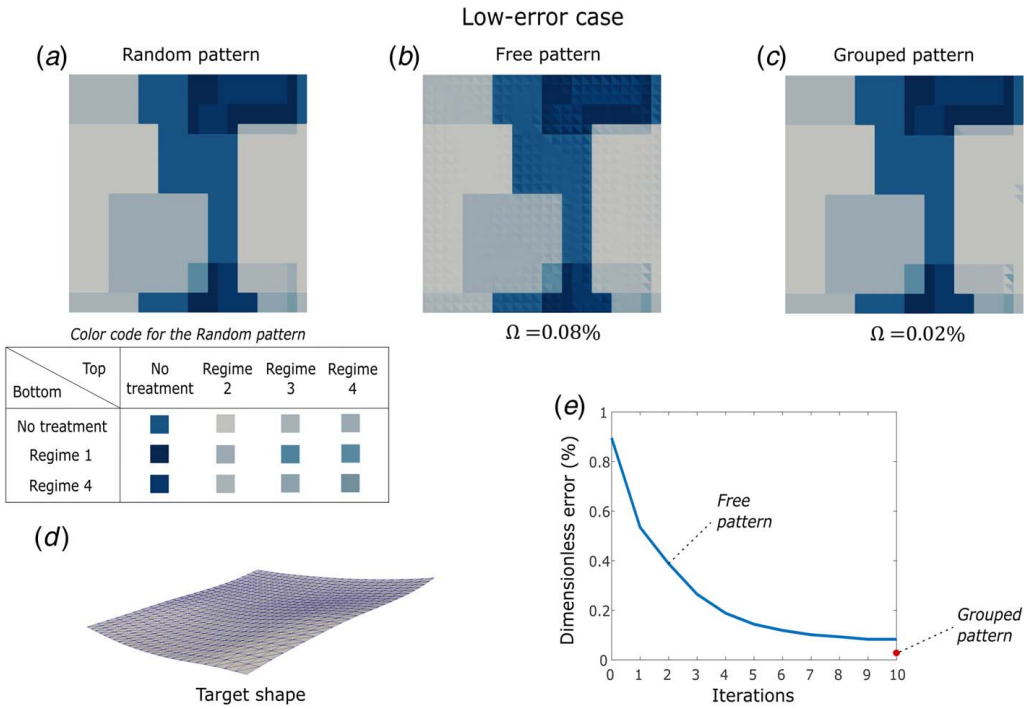

Fig. 9 One of the test cases from series 2 with low dimensionless error. The plate is 7 mm thick, and the Poisson's ratio equals 0.34. (*a*) The random peening pattern generated for this test case (top layer). The applied peening regimes are those summarized in Table 1. (*b*) The free peening pattern on the final iteration. (*c*) The grouped peening pattern. A visual comparison of (*c*) and (*a*) shows that almost all elements were attributed to a correct group. Consequently, grouping decreased the dimensionless error Ω. (*d*) The target shape induced by the pattern (*a*). The deformations are at their original scale. (*e*) The convergence curve showing the dimensionless error Ω on each iteration. The optimization required 10 iterations that was the maximum fixed for this test.

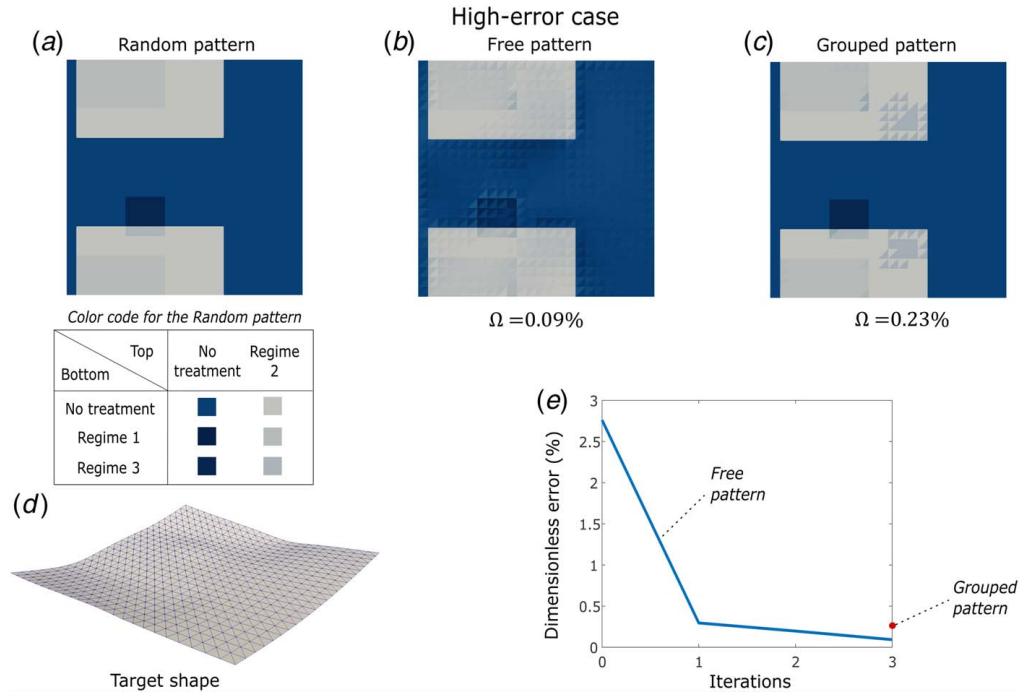

Fig. 10 One of the test cases from series 2 with high dimensionless error. The plate is 4 mm thick, and the Poisson's ratio equals 0.34. (*a*) The random peening pattern generated for this test case (top layer). The applied peening regimes are those summarized in Table 1. (*b*) The free peening pattern on the final iteration. (*c*) The grouped peening pattern. A visual comparison of (*c*) and (*a*) indicates elements that were not attributed to a correct group. Consequently, grouping increased the dimensionless error Ω in this case. The deformations are at their original scale. (*d*) The target shape induced by the pattern (*a*). (*e*) The convergence curve showing the dimensionless error Ω on each iteration. The optimization required three iterations to converge.

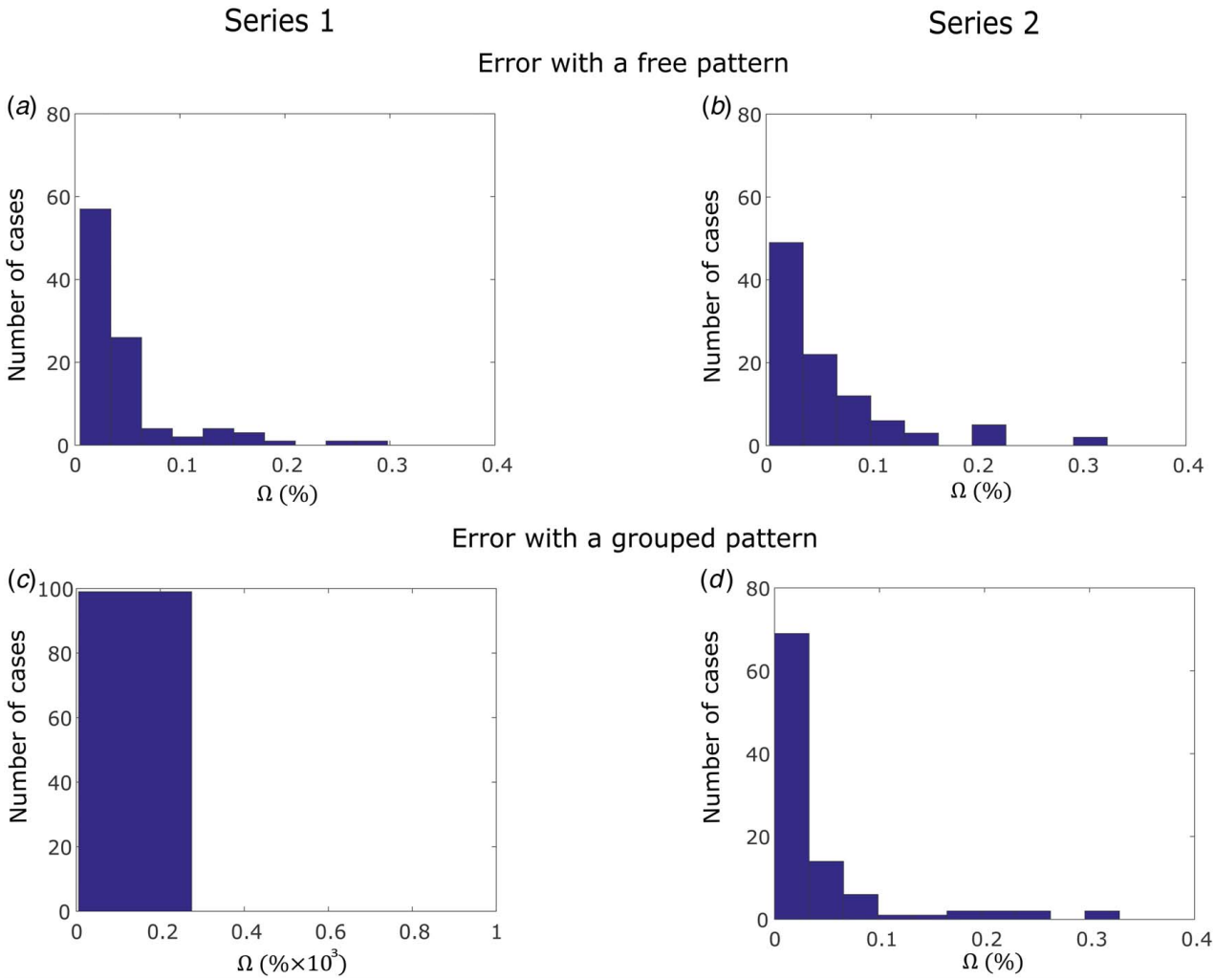

Fig. 11 Histograms evaluating the dimensionless error Ω between the target shapes and the final shapes obtained during the numerical validation of the inverse problem solver. All in all, 200 test cases were considered. They were divided into two series of 100 cases each. The target shapes in series 1 were obtained with one peening regime, and the same peening regime was fixed as the only available for the grouping stage. The target shapes in series 2 were obtained with four different peening regimes, and the four predefined regimes were available for grouping. Figures (*a*) and (*b*) show the dimensionless error induced by application of the free pattern for series 1 and 2 correspondingly. Similarly, figures (*c*) and (*d*) represent the dimensionless error induced by the grouped pattern.

solution does not converge to the exact target shape but to a shape which is close to the target. Thus, when computing an eigenstrain adjustment for each element, the iterative algorithm does not take into account the influence of the eigenstrain adjustments prescribed to the neighboring elements on the stretching and curvature of this element. Consequently, after several iterations, the Ω plateaus at a low but finite level (Figs. 9(*e*) and 10(*e*)). The Ω may slightly grow during the subsequent iterations, but the stop criterion (27) terminates the iterative process as soon as this happens. Decreasing the threshold δ (see Eq. (23)) during the adjustment phase allows to converge closer to the target shape but increases the number of iterations required.

The results of the numerical validation are presented with histograms in Fig. 11. The inverse problem solver provided free peening patterns that led to the target shape with the Ω inferior to 0.35% for both series of tests (Fig. 11, top). The pattern optimization needed between 2 and 10 iterations, depending on the target shape.

The histograms in Fig. 11 show that the pattern grouping has decreased the Ω in most of the cases. Thus, the original pattern was perfectly reproduced for all test cases in series 1, so the Ω after grouping became less than 10^{-3}%. The corresponding Ω for series 2 was bigger because of the higher complexity of the grouping problem: four available regimes induced 25 group centroids for series 2, while there were only four centroids induced by one available regime for series 1. The group centroids for series 2 were situated close to each other, so several test cases were significantly affected by the checkerboard problem, as illustrated in Fig. 10(*c*). This explains the increased error after grouping for 18 cases out of 100 from series 2.

5 Discussion

The described inverse problem resolution algorithm relies on the assumption that the peening treatment induces isotropic expansions. In practice, however, peen forming sometimes induces different eigenstrain along the x and y axes: $\varepsilon_{xx}(x, y, z) \neq \varepsilon_{yy}(x, y, z)$. Such anisotropic expansions are due to plastic anisotropy of the treated material, which is especially explicit for rolled aluminum sheets, and for prestressing the component in one direction before treatment, i.e., stress peen forming. This effect is examined in detail in Ref. [32]. For uniform plastic anisotropy which does not vary over the area of the plate, the inverse problem resolution algorithm can be easily adapted by introducing a fixed eigenstrain anisotropy

coefficient χ in the model:

$$\varepsilon^j_{xx} = \frac{(1+\chi)}{(1-\chi)}\varepsilon^j_{yy} \quad \text{for } j = t, b \tag{36}$$

This relation may be imposed after adjustment of the bilayer rest fundamental forms $\mathbf{a}_{r,t}$ and $\mathbf{a}_{r,b}$ on each iteration. Thus, the forward problem will be solved taking into account the plastic anisotropy.

The residual stresses generated in the structure by the prescribed peening treatment can be evaluated after the grouping phase. Indeed, if each available peening regime is experimentally characterized in terms of the induced through-thickness eigenstrain profile [7,24], then, at each point (x_0, y_0), the local elastic strain profile $\boldsymbol{\varepsilon}^{\text{el}}(x_0, y_0, z)$ can be computed by subtracting the eigenstrain profile $\boldsymbol{\varepsilon}(x_0, y_0, z)$ from the residual strain profile $\boldsymbol{\varepsilon}^{\text{res}}(x_0, y_0, z)$ (see Eq. (1)). The local residual stress profile $\boldsymbol{\sigma}(x_0, y_0, z)$, in turn, can be deduced from $\boldsymbol{\varepsilon}^{\text{el}}(x_0, y_0, z)$ using Eq. (6).

The forming influence of the initial stresses, which are present in the structure before shot peening, can also be taken into account. Thus, if the through-thickness profile of initial stresses is measured [32], then a through-thickness eigenstrain profile inducing the measured initial stresses can be computed [24]. The idealized formulation of the initial eigenstrain profile can then be represented in terms of ε^t and ε^b using the equality between the total eigenstrains (see Eqs. (2) and (4)) and the first eigenstrain moments (see Eqs. (3) and (5)). Therefore, the computed ε^t and ε^b corresponding to the initial stresses can be subtracted from $\varepsilon^{rf,t}$ and $\varepsilon^{rf,b}$, respectively, on the final stage of the iterative algorithm.

Given that the rest fundamental forms are numerically adjusted for each triangular element separately, the efficiency of the inverse problem resolution depends on the consistency between the target mesh and the initial mesh. More precisely, it depends on the mapping $\vec{m}$ between the initial 2D shape and the target 3D shape. The general requirement for the mapping is to preserve the shape of each triangular element as well as possible. This minimizes the local eigenstrain assigned by the algorithm and makes the computed free pattern smoother. This problem was not faced during the numerical validation because the target shapes were derived from the initial shapes through the forward problem resolution, so they were optimally meshed by default.

The mesh consistency can be ensured by fixing the target shape mesh and by its mapping onto the initial 2D geometry. The fixed initial geometry is an important constraint for the mapping because it involves a fixed 2D boundary. The mapping can be done using the methods oriented on maximal preservation of local angles, such as the least squares conformal mapping algorithm [33]. Next, local mesh distortions with respect to the target mesh can be minimized using a numerical optimization algorithm. For example, the L-BFGS algorithm that we use for the global elastic energy minimization can cope with this task.

Finally, the proposed grouping strategy relies on the fact that set of N experimentally characterized peening regimes is fixed, which limits the range of available target shapes. Hence, an automated determination of the optimal peening regimes for each target shape would expand this range. In addition, if the optimal regimes are computed in terms of eigenstrains, then a method for reconstructing the process parameters from the required eigenstrains must be found.

6 Conclusion

The theory of non-Euclidean plates in combination with the eigenstrain approach provides an extensive theoretical framework for the modeling of shot peen forming. The eigenstrain approach represents the treated plate as a bilayer undergoing nonuniform eigenstrain, and the theory of non-Euclidean plates accurately solves the forward problem for this case. The deformed shape is calculated through minimization of the global elastic energy following analytical gradients.

The iterative inverse problem resolution is based on the comparison of geometrical properties of the plate in its current and target configurations. The adjustment of the prescribed eigenstrain on each iteration is done on a local scale involving simple arithmetic operations and takes negligible amount of time. A low number of iterations (not more than 10) ensures fast resolution of the inverse problem. According to the numerical validation, the inverse problem resolution algorithm computes free peening patterns that shape 1×1 m aluminum plates of various thicknesses into freeform shapes with a tolerance of 3.5 mm. The precision of the inverse problem resolution is, however, dependent on consistency between the initial and the target meshes.

The eigenstrain formulation of the inverse problem makes the algorithm applicable for any type of processes that induce small isotropic eigenstrain. These include, among others, laser peen forming of metal plates or 4D printing of shape-shifting polymer structures.

The pattern grouping makes the inverse problem solution practically applicable. It adds uncertainty to the solution, but in many cases it decreases the induced error. The grouping algorithm can locally mix up the peening regimes having slightly different intensities. A method for correction of the local grouping errors would enhance the solution quality.

The future work implies experimental validation of the proposed inverse problem simulation technique. It will reveal practical constraints that may cause simulation error. Among others, we will examine influence of the peening parameters and of the material plastic anisotropy on the induced eigenstrain.

Acknowledgment

The authors gratefully acknowledge financial support from The Fonds de recherche du Québec – Nature et technologies (FRQNT) and The Aluminium Research Center (REGAL).

Conflict of Interest

There are no conflicts of interest.

Data Availability Statement

The data and information that support the findings of this article are freely available.[2]

Nomenclature

h = plate thickness
$\vec{m}$ = mapping defining position of each point of the mid-surface in $\mathbb{R}^3$ based on its coordinates in U
$\vec{n}$ = unit normal vector
$\vec{r}$ = radius-vector defining position of each point of the plate in space
z = through-thickness coordinate
$\mathbf{a}$ = 2×2 matrix defining the local first fundamental form
$\mathbf{b}$ = 2×2 matrix defining the local second fundamental form
K = number of triangular elements in the model
M = maximal number of iterations
N = number of predefined peening regimes
U = domain of $\mathbb{R}^2$ englobing the plate mid-surface in coordinates (x, y)
Y = Young modulus
$\mathbf{I}$ = identity matrix
$\mathbf{S}$ = shape operator
d_H = Hausdorff distance

[2] https://github.com/lm2-poly/peen_forming_2022

k_A = ratio between the target local area and the current local area
k_H = ratio between the target local mean curvature and the current local mean curvature
A_c = current local area
A_{tar} = target local area
A_{total} = total area of the plate in its initial configuration
$\mathcal{C}_c$ = point cloud describing the current configuration
$\mathcal{C}_f$ = point cloud describing the final configuration
$\mathcal{C}_{\text{tar}}$ = point cloud describing the target configuration
E_{BL} = elastic energy of a bilayer
E_{ML} = elastic energy of a monolayer
H_c = current local mean curvature
H_{tar} = target local mean curvature
U_1 = sub-domain of U
$\mathbf{S}_c$ = current shape operator
$\mathbf{S}_r$ = rest shape operator
$\mathbf{S}_{\text{tar}}$ = target shape operator
$\mathcal{C}_c^{\text{new}}$ = point cloud describing the current configuration obtained by assignment of the adjusted rest configuration and subsequent deformation
$\mathbf{S}_r^{\text{new}}$ = adjusted rest shape operator
$(\mathbf{a}_{r,t}, \mathbf{a}_{r,b})$ = two first fundamental forms defining the bilayer rest configuration
$(\mathbf{a}_{r,t}^{\text{ortho}}, \mathbf{a}_{r,b}^{\text{ortho}})$ = two first fundamental forms defining the bilayer rest configuration for the case of local in-plane orthotropic growth
$(\mathbf{a}_{r,t}^{\text{new}}, \mathbf{a}_{r,b}^{\text{new}})$ = two first fundamental forms defining the adjusted bilayer rest configuration
$(\mathbf{a}_{rf,t}, \mathbf{a}_{rf,b})$ = two first fundamental forms defining the bilayer rest configuration obtained on the final iteration
$(\mathbf{a}_c, \mathbf{b}_c)$ = first and the second fundamental forms defining the monolayer current configuration
$(\mathbf{a}_c^{\text{new}}, \mathbf{b}_c^{\text{new}})$ = first and the second fundamental forms defining the monolayer current configuration, which was obtained by assignment of the adjusted rest configuration and subsequent deformation
$(\mathbf{a}_f, \mathbf{b}_f)$ = first and the second fundamental forms defining the monolayer final configuration
$(\mathbf{a}_{\text{init}}, \mathbf{b}_{\text{init}})$ = first and the second fundamental forms defining the monolayer initial configuration
$(\mathbf{a}_r, \mathbf{b}_r)$ = first and the second fundamental forms defining the monolayer rest configuration
$(\mathbf{a}_r^{\text{new}}, \mathbf{b}_r^{\text{new}})$ = first and the second fundamental forms defining the adjusted monolayer rest configuration
$(\mathbf{a}_r^{\text{ortho}}, \mathbf{b}_r^{\text{ortho}})$ = first and the second fundamental forms defining the monolayer rest configuration for the case of local in-plane orthotropic growth
$(\mathbf{a}_{\text{tar}}, \mathbf{b}_{\text{tar}})$ = first and the second fundamental forms defining the monolayer target configuration
$\vec{e}_0, \vec{e}_1, \vec{e}_2$ = edge vectors defining three edges of a triangular element
$\vec{n}_0, \vec{n}_1, \vec{n}_2$ = edge directors defining normals to the three edges of a triangular element
$\vec{v}_0, \vec{v}_1, \vec{v}_2$ = position vectors defining three vertices of a triangular element
(x, y) = Lagrangian curvilinear coordinates parametrizing the plate mid-surface
Γ = total eigenstrain
Γ_1 = first eigenstrain moment
δ = upper threshold for $|k_H|$
$\boldsymbol{\varepsilon}$ = eigenstrain tensor induced by the peening treatment
$\boldsymbol{\varepsilon}^{\text{el}}$ = strain tensor reflecting the elastic material response
$\boldsymbol{\varepsilon}^{\text{res}}$ = residual strain tensor
$(\varepsilon^t, \varepsilon^b)$ = eigenstrain induced in the top and bottom layers of a bilayer, respectively
$(\varepsilon_{\text{avg}}^t, \varepsilon_{\text{avg}}^b)$ = average of the orthotropic eigenstrain in two principal directions on the top and bottom layers, respectively
$(\varepsilon^{\text{cen},t}, \varepsilon^{\text{cen},b})$ = a group centroid on the plane $(\varepsilon^t, \varepsilon^b)$
$(\varepsilon^{rf,t}, \varepsilon^{rf,b})$ = eigenstrain prescribed to the top and bottom layers by $(\mathbf{a}_{rf,t}, \mathbf{a}_{rf,b})$
(θ^t, θ^b) = angles between the local principal strain direction and the x axis on the top and bottom layers, respectively
ν = Poisson's ratio
$\boldsymbol{\sigma}$ = residual stress tensor
τ = threshold for the dimensionless error between the current and the target configurations used as a stop condition
$\varphi_0, \varphi_1, \varphi_2$ = angles of inclination of the edge-director vectors $\vec{n}_0, \vec{n}_1, \vec{n}_2$ with respect to the average of the adjacent face normals
Ω = dimensionless error between the final and the target configurations

References

[1] Ramati, S., Kennerknecht, S., and Levasseur, G., 1999, "Single Piece Wing Skin Utilization Via Advanced Peen Forming Technologies," Proceedings of the 7th International Conference on Shot Peening (ICSP7), Warsaw, Poland, Sept. 28–30.
[2] de los Rios, E., Walley, A., Milan, M., and Hammersley, G., 1995, "Fatigue Crack Initiation and Propagation on Shot-Peened Surfaces in A316 Stainless Steel," Int. J. Fatigue, **17**(7), pp. 493–499.
[3] Faucheux, P. A., 2019, "Simulating Shot Peen Forming With Eigenstrains," Ph.d. dissertation, Polytechnique Montreal, Montreal, December.
[4] Chen, Z., Yang, F., and Meguid, S., 2014, "Realistic Finite Element Simulations of Arc-Height Development in Shot-Peened Almen Strips," J. Eng. Mater. Technol., **136**(4), p. 041002.
[5] Mura, T., 1987, *Micromechanics of Defects in Solids*, Springer Science & Business Media, Dordrecht, p. 21.
[6] Korsunsky, A. M., 2005, "The Modelling of Residual Stresses Due to Surface Peening Using Eigenstrain Distributions," J. Strain Anal. Eng. Des., **40**(8), pp. 817–824.
[7] Faucheux, P. A., Gosselin, F. P., and Lévesque, M., 2018, "Simulating Shot Peen Forming With Eigenstrains," J. Mater. Process. Technol., **254**, pp. 135–144.
[8] Siguerdidjane, W., Khameneifar, F., and Gosselin, F. P., 2020, "Efficient Planning of Peen-Forming Patterns Via Artificial Neural Networks," Manuf. Lett., **25**, pp. 70–74.
[9] Pajot, J. M., Maute, K., Zhang, Y., and Dunn, M. L., 2006, "Design of Patterned Multilayer Films With Eigenstrains by Topology Optimization," Int. J. Solids Struct., **43**(6), pp. 1832–1853.
[10] Miao, H. Y., Lévesque, M., and Gosselin, F. P., 2022, "Shot Peen Forming Pattern Optimization to Achieve Cylindrical and Saddle Target Shapes: The Inverse Problem," CIRP J. Manuf. Sci. Technol., **36**, pp. 67–77.
[11] Luo, M., Hu, Y., Hu, L., and Yao, Z., 2020, "Efficient Process Planning of Laser Peen Forming for Complex Shaping With Distributed Eigen-Moment," J. Mater. Process. Technol., **279**, p. 116588.
[12] Efrati, E., Sharon, E., and Kupferman, R., 2009, "Elastic Theory of Unconstrained Non-Euclidean Plates," J. Mech. Phys. Solids, **57**(4), pp. 762–775.
[13] Efrati, E., Sharon, E., and Kupferman, R., 2013, "The Metric Description of Elasticity in Residually Stressed Soft Materials," Soft Matter, **9**(34), pp. 8187–8197.
[14] Pezzulla, M., Shillig, S. A., Nardinocchi, P., and Holmes, D. P., 2015, "Morphing of Geometric Composites Via Residual Swelling," Soft Matter, **11**(29), pp. 5812–5820.
[15] Pezzulla, M., Smith, G. P., Nardinocchi, P., and Holmes, D. P., 2016, "Geometry and Mechanics of Thin Growing Bilayers," Soft Matter, **12**(19), pp. 4435–4442.
[16] Chen, H.-Y., Sastry, A., van Rees, W. M., and Vouga, E., 2018, "Physical Simulation of Environmentally Induced Thin Shell Deformation," ACM Trans. Graph., **37**(4), pp. 1–13.
[17] van Rees, W. M., Matsumoto, E. A., Gladman, A. S., Lewis, J. A., and Mahadevan, L., 2018, "Mechanics of Biomimetic 4D Printed Structures," Soft Matter, **14**(43), pp. 8771–8779.
[18] Aharoni, H., Xia, Y., Zhang, X., Kamien, R. D., and Yang, S., 2018, "Universal Inverse Design of Surfaces With Thin Nematic Elastomer Sheets," Proc. Natl. Acad. Sci. U.S.A., **115**(28), pp. 7206–7211.
[19] van Rees, W. M., Vouga, E., and Mahadevan, L., 2017, "Growth Patterns for Shape-Shifting Elastic Bilayers," Proc. Natl. Acad. Sci. U.S.A., **114**(44), pp. 11597–11602.
[20] Klotz, T., Delbergue, D., Bocher, P., Lévesque, M., and Brochu, M., 2018, "Surface Characteristics and Fatigue Behavior of Shot Peened Inconel 718," Int. J. Fatigue, **110**, pp. 10–21.
[21] Rossini, N., Dassisti, M., Benyounis, K., and Olabi, A.-G., 2012, "Methods of Measuring Residual Stresses in Components," Mater. Des., **35**, pp. 572–588.
[22] Flavenot, J. F., and Niku-Lari, A., 1977, "La mesure des contraintes résiduelles. Méthode de la flèche. Méthode de la source des contraintes. Application au grenaillage de précontrainte et à d'autres traitements superficiels," Tech. Rep. 31, CETIM, Senlis, France, September.

[23] Prime, M. B., and Hill, M. R., 2002, "Residual Stress, Stress Relief, and Inhomogeneity in Aluminum Plate," Scr. Mater., **46**(1), pp. 77–82.
[24] Korsunsky, A. M., 2006, "Residual Elastic Strain Due to Laser Shock Peening: Modelling by Eigenstrain Distribution," J. Strain Anal. Eng. Des., **41**(3), pp. 195–204.
[25] Ciarlet, P. G., 2005, "An Introduction to Differential Geometry With Applications to Elasticity," J. Elast., **78**(1), pp. 1–215.
[26] Spivak, M., 1975, *A Comprehensive Introduction to Differential Geometry*, Vol. 3, Publish or Perish, Boston, MA.
[27] Weischedel, C., Tuganov, A., Hermansson, T., Linn, J., and Wardetzky, M., 2012, "Construction of Discrete Shell Models by Geometric Finite Differences," Fraunhofer ITWM, Kaiserslautern.
[28] Liu, D. C., and Nocedal, J., 1989, "On the Limited Memory BFGS Method for Large Scale Optimization," Math. Program., **45**(1), pp. 503–528.
[29] Tamstorf, R., and Grinspun, E., 2013, "Discrete Bending Forces and Their Jacobians," Graph. Models, **75**(6), pp. 362–370.
[30] van Rees, W. M., 2018, "Code Accompanying the 2018 Soft Matter Paper "Mechanics of Biomimetic 4D Printed Structures," https://github.com/wimvanrees/growth_SM2018
[31] Besl, P., and McKay, N. D., 1992, "A Method for Registration of 3-D Shapes," IEEE Trans. Pattern Anal. Mach. Intell., **14**(2), pp. 239–256.
[32] Faucheux, P. A., Miao, H. Y., Lévesque, M., and Gosselin, F. P., 2022, "Peen Forming and Stress Peen Forming of Rectangular 2024-T3 Aluminium Sheets: Curvatures, Natural Curvatures and Residual Stresses," Strain, **58**(2), p. e12405.
[33] Lévy, B., Petitjean, S., Ray, N., and Maillot, J., 2002, "Least Squares Conformal Maps for Automatic Texture Atlas Generation," ACM Trans. Graph., **21**(3), pp. 362–371.